Multiaxial loading of aeronautic composite structures at intermediate scale: A review of VERTEX developments

Bruno Castanié, Jean-Charles Passieux, Jean-Noël Périé, Christophe Bouvet, John-Eric Dufour, Joël Serra

Multiaxial loading of aeronautic composite structures at intermediate scale: A review of VERTEX developments

Bruno Castanié , Jean-Charles Passieux , Jean-Noel Périé , Christophe Bouvet , John-Eric Dufour , Joël Serra

PII: S2666-6820(24)00010-0
DOI: https://doi.org/10.1016/j.jcomc.2024.100439
Reference: JCOMC 100439

To appear in: *Composites Part C: Open Access*

Received date: 15 January 2024
Accepted date: 27 January 2024

Please cite this article as: Bruno Castanié , Jean-Charles Passieux , Jean-Noel Périé , Christophe Bouvet , John-Eric Dufour , Joël Serra , Multiaxial loading of aeronautic composite structures at intermediate scale: A review of VERTEX developments, *Composites Part C: Open Access* (2024), doi: https://doi.org/10.1016/j.jcomc.2024.100439

Multiaxial loading of aeronautic composite structures at intermediate scale:

A review of VERTEX developments.

Bruno Castanié[1,*], Jean-Charles Passieux[1], Jean-Noel Périé[1], Christophe Bouvet[1], John-Eric Dufour and Joël Serra[1]

[1]Institut Clément Ader. ISAE-SUPAERO – INSA – IMT Mines Albi – UPS – CNRS, Toulouse, France.

*corresponding author: bruno.castanie@insa-toulouse.fr

Abstract

The certification of aeronautical composite structures is based on a pragmatic approach, which is intended to be safe and essentially experimental but with a strong test/calculation dialogue called the "Test Pyramid". However, this has proved to be extremely expensive and it appears necessary to reduce its cost either by developing Virtual testing, or by developing richer tests on an intermediate scale between coupon specimens and structural parts. It was in the aim of meeting this objective that the VERTEX program (French acronym for "Experimental modeling and Validation of compositE strucTures under complEX loading") was launched in 2012. After positioning the VERTEX program in relation to the literature, this review will explain the methodology and present the measurement methods specifically developed for this scale. Then, three scientific themes that have been studied will be detailed (large notches, impact and wrinkling case studies). Finally, a proposal for validating the structures using envelope curves will be put forward, an assessment made, and perspectives presented.

Keywords: Testing; Multiaxial loading; Digital image Correlation; Composite Structures

1. Introduction

The certification of aeronautical composite structures is based on a pragmatic approach, which is intended to be safe. It is essentially experimental but uses a strong test/calculation dialogue called the "Test Pyramid" (Figure 1, [1, 2]). The first level of the pyramid is that of coupon tests, which make it possible to obtain the admissible values for the current sections, the junctions and the impact, considering the environmental effects (temperatures and humidity) and also the dispersion (A values and B values) [3]. At higher levels, the structural details, then the subassemblies and, finally, the complete aircraft must be validated. An example of the number and complexity of such structural tests used by NASA for the validation of a carbon wing box during the Advanced Composites Technology (ACT) Program [4] is given in Figure 2. It can also be noted that these tests are uniaxial, while the structures are subjected to multiaxial constraints. In total, several tens of thousands of tests are carried out during programs such as those of the BOEING 787 or the AIRBUS A350. The costs associated with this approach are very high and generate very long design cycle times. In addition, many problems can only be detected during late structural tests, and thus generate significant additional costs. *There is therefore a need to develop a standard testing methodology at scales greater than coupons but without going into the complexity of the structural details shown in Figure 2* [3]. This is what we will call the intermediate scale. In addition, deep knowledge of the structural response early in the aircraft program makes it possible to develop and make digital models that will become more reliable by being part of a Virtual Testing Approach.

A literature review of various testing bench technologies that make it possible to satisfy this need have already been presented in [5] and [6] and are just summarized here. There are generally two families of test benches allowing multiaxial loading of panels. The first directly loads the plate, via series of jacks, onto a simplified frame in which the panel is fixed [7-12]. The main advantage of this type of test bench is its structural simplicity (Figure 3 (a) and (b)). More recently, modular assemblies, which make it possible to test a large number of structures, possibly in several fields (Automobile, Wind Energy, Aeronautics, etc.), have been selected by various research organizations [7-9]. They also make it easier to carry out fatigue tests at the structure scale. However, most often, a large number of actuators must be used to carry out multiaxial tests, as in the case of the FAA's FASTER (Full-Scale Aircraft Structural Test Evaluation and Research) facility, which involves complex piloting of the test [10]. In addition, the decoupling of forces requires specific solutions that are also complex [11]. Another way of loading panels under complex loads is the use of boxes. This principle was first used by Peters [13] in 1948 to test aeronautical plates under combined stresses. It has been taken up numerous times on more or less significant scales, for example by the DLR [14] or by NASA, Langley, via its gigantic COLTS loading system (COmbined Loading Testing System, [15]). COLTS uses a D-Box to enable large curved panels to be loaded under shear, compression-tension and internal pressure [16]. At a small scale, in the 1990s, Castanié et al. [17, 18] used the box principle to test asymmetric sandwich structures in compression and shear and/or combined compression/shear. The loading principle and the design were validated by these studies but it was noted that the zone of interest (200 x 200 mm2) was too small and generated a lot of boundary Saint-Venant effects. Furthermore, as found by Klein [14], it was difficult to evaluate the stress flows entering the test specimen due to structural redundancies. Therefore, the development of this type of structural testing requires the simultaneous development of specific measurement strategies. Finally, asymmetrical

sandwich specimens having been tested under stress after impact [18], it was noted that the failure scenarios were very different and more progressive than in the case of the standardized specimens habitually used [19]. This type of test can therefore provide less conservative design values by employing loading modes and boundary conditions closer to the reality of structures. Following up on such considerations in partnership with industrial partners led to the development of a machine based on the box principle during the "VERTEX" research program. VERTEX is the French acronym for "Experimental modeling and **V**alidation of composit**E** st**R**uc**T**ures under compl**EX** loading".

In the following section, the operating principle of the machine and the main points of development will be recalled. In this type of structure, it may be interesting to know the direct relationship between the forces applied and the stresses in the specimen. Such a transfer law has recently been found via an explicit nonlinear modeling of the assembly and the findings will be presented briefly. The following section is dedicated to the specific measurement methods developed during these 10 years of study. Then some case studies, i.e. large notch, impact, and wrinkling will be presented, in this order. A paragraph is then dedicated to the concept of failure envelopes, which are allowed by this means of testing. The paper will conclude with a succinct presentation of current studies, an assessment of the contribution of the VERTEX method, and perspectives.

2. The VERTEX Test Bench

The specifications after a benchmark with aeronautics manufacturers made it possible to establish a maximum load envelope: 3000 N/mm in traction or compression, 1000 N/mm in shear, and an internal pressure of 1.6 bars. The principle of the machine is shown in Figures 5 and 6. The specimen is bolted onto the upper part of the central box located between the two IPN transversal beams. When jacks 1 and 2 are activated, the whole longitudinal box is subjected to 4-point bending and therefore the specimen can be loaded under tension or

compression. When jacks 3 and 4 are activated, the central box is twisted and the sample is thus subjected to shear. Of course, these four jacks can also be used in combinations.

The area of interest was quadrupled to 400 x 400 mm^2, which typically corresponds to the size of one or two bays (the inter-frame and inter-stiffener areas). The laboratory has a large reaction table on which the assembly could be fixed but which imposes space constraints. The details of the sizing and load cases are given in [5] and the final assembly can be seen in Figure 7. The overall dimensions are 8.5 m length, 2.9 m width and 3 m height. The box itself is 0.5 m high. 128 bolts are used to fasten the specimen on the central box and to sustain the maximum loads (Figure 8(a)), which leads to an overall size of the specimen, including the bolting area, of 558 mm × 536 mm. An air-pressurized rubber bladder (Fig. 8(b)) can be added in the central box to load the sample with pressure. The cost of this assembly (studies, manufacture and assembly) was about 500 k€. Recently [6], a significant effort was made to obtain a comprehensive model of the test bench because a detailed FEM is needed to determine the link between the displacements of the four actuators and the load (amplitude and shape) actually applied to the specimen. This difficulty is not specific to the VERTEX machine; it occurs every time a large test rig is used. Therefore, the modeling strategy to simulate the behavior of a complex test rig (choice of type of finite elements, connections, contact, solver) has been described. More specifically, attention was paid to the modeling of the bolted joint, especially between the specimen and the VERTEX test bench. The relative influences of the stiffnesses (axial/radial) of the junctions of the machine according to their location (Sample/Box/Beam) have been obtained and an explanation of the internal coupling observed (transverse compression associated with longitudinal tension when “tension” jacks 1-2 are used and the longitudinal tension associated with shear when “shear” jacks 3-4 are used) is provided. Now this explicit model allows us to predict:

- the bearing loads,

- the sample shape to delay secondary corner failures and failure assessment using a simple strain criterion.
- the response of the sample for complex loading paths
- the sizing of new specimens like impacted stiffened panels [20]

The specific measurement strategy will be described in the next sections.

3. Stereo-DIC Measurements for estimating boundary conditions and loading

Obtaining boundary conditions and loading for direct use in FE simulations was one of the main motivations for the DIC developments presented here. The assembly is indeed highly hyperstatic and the only static quantities available are the forces applied by the actuators. Consequently, due to the multitude of load paths (structural redundancy) connecting the actuators to the specimen, the relationship between the force applied by the actuators and the load applied to the specimen is not trivial. In addition, as the specimen is part of the test rig itself, it influences the overall stiffness of the machine. Therefore, an in-situ measurement was essential to accurately assess the load applied to the specimen. In the seminal work of Castanié [18, 19], the periphery of the useful zone of the specimen was used to estimate the load applied to the specimen and its distribution along the edges of the FE model. This part of the specimen was then considered as a spring element and its deformation was evaluated by a few gauges glued face to face on the two faces of the plate. However, the sparseness of these measurements required new assumptions to be made in order to provide the simulation with a load distribution. Furthermore, these measurements did not give access to the initial geometry of the specimen, nor to its modification after its installation in the machine, and even less to a kinematic field that could be used as a Dirichlet boundary condition for the numerical simulation. In addition to the boundary conditions and load estimation, the aim was also to provide well-resolved full-field kinematic measurements for comparison and, ultimately,

control purposes [21, 22, 23]. For example, in the case of a notched specimen, the goal was to capture the strain fields in the vicinity of the notch tip instead of a set of gauge measurements. For these reasons, with the new Vertex bench, it was decided to move to digital image correlation (DIC) measurements to fill these gaps and complement the strain gages. However, there were major obstacles in the way. In particular, the expected resolution of the DIC strain measurement made it unrealistic to attempt a correct estimation of the load distribution around the useful region using small optical strain gauges. For this reason, a multi-resolution camera cluster was preferred.

3.1 State of the art of stereo DIC based boundary conditions and loading measurements at the beginning of the Vertex project

The software that was used for this type of processing was VIC 3D. It is based on the conventional approach to stereo correlation, i.e. on a "subset" approach [24]. Points in one of the two stereoscopic images (say, the left image) are matched to their counterparts in the second (say, the right image). The 3D coordinates of the corresponding 3D points are computed using triangulation. The result is a point cloud that describes the shape of the object. The operation is then repeated for the next deformation step. The result is a new point cloud describing the new shape of the object. The displacement field is then obtained by simply comparing the two previous point clouds. This approach is particularly robust and processing is fast.

The mean stresses were first determined by laminate theory from the strains obtained by SDIC (here VIC3D), averaged over the blue zones at the edge of the zone of interest of the specimen. The ‘‘global” strains ($\varepsilon_{xx\ ,\ global}$ and $\varepsilon_{xy\ ,\ global}$) were determined by dividing the displacements measured at extreme points by the distance separating them (virtual extensometer). The processing of these averaged stresses was first carried out assuming that

the plate was undergoing only membrane stresses. In this case, the strains are constant through the thickness. This assumption holds when specimens are tested under tension but leads to erroneous information when bending is triggered by either compressive or shear loading. Local curvatures therefore needed to be accounted for.

Using classical plate theory and full-field measurements of the stereo-correlation, force fluxes and moment fluxes can be computed from: upper-skin strain measurements, out-of-plane displacement measurements, and the assumed stiffness of the plate (Figure 9). The latter is computed from ply thicknesses, layup, and ply material values. Figure 10 shows all flux fields computed on most of the area of interest, with a 5 mm step between points. A simple description of the temporal evolution of fluxes requires each spatial field to be aggregated into a representative scalar so that it can be plotted against time. For a given frame captured by cameras, flux fields are computed, then a scalar representative of border fluxes is computed for each field by averaging the flux values contained in the blue boxes of Figure 10.

The subset-based DIC procedure described above presents several limitations. First, displacement is the result calculated for several successive inverse problems. Furthermore, the nature of such measurements and the reference frame in which they are expressed do not allow them to be used directly to establish a dialogue with FE simulations. Some assumptions, interpolations or approximations are necessary, for example, just to run an FE simulation with experimental boundary conditions. For instance, in [25], a special projection and separation of in-plane and out-of-plane displacements in a band of elements was required to apply measured displacements and rotations to the boundaries of a plate model. In addition, with such an indirect formulation, prescribing regularization of the displacement field or simply performing data assimilation (namely integrating measurements with FE models) is hardly feasible. For all these reasons, we decided to develop a completely new global approach to DIC stereo.

3.2 FE based stereo DIC

To directly extract the quantities of interest, i.e. the loading and the boundary conditions, the idea was to integrate the relevant mechanical information (e.g. elasticity) a priori, rather than having to post-process noisy DIC measurements. However, as mentioned above, conventional (subset-based) stereo DIC techniques [24] were not compatible with this kind of non-local regularizations that would couple all the subsets. In addition, people are used to relying on finite elements to build stiffness operators in solid mechanics. All this led us to develop a new finite element approach to stereo DIC, the main components of which are outlined below. As will be shown, it becomes possible to integrate the model, weakly or strongly, directly into the measurements. In addition, this approach has the merit of opening up a number of interesting avenues. For example, the potential of the technique for multi-sensor and multi-resolution data fusion is illustrated in this section. In addition to the main limitations mentioned above, classical subset DIC [24] also had a number of minor disadvantages that were corrected by the proposed version of the finite element approach.

First, because classical DIC was originally inspired by computer vision, the working units are in pixels and the working coordinate system is that of the image. Switching from a pixel displacement field in an image coordinate system to the specimen coordinate system is not necessarily a complex post-process but, from a mechanic's point of view, we thought it was much more convenient to formulate the DIC problem in the coordinate system of the real part, with physical units and a much more direct comparison with the simulation.

Secondly, in stereo DIC, the formulation is asymmetric. There is a primary (master) camera and a secondary (slave) camera. However, there is no reason why this should be the case. More importantly, the classical formulation of stereo DIC works with two cameras. This is a limitation because, in structural tests such as Vertex, given the multiscale nature of the physics, it was relevant to consider multiple cameras focusing at different scales - from tens

of mm to half a meter. We have developed a DIC framework that can naturally and seamlessly merge images from any number of cameras within a single multi-camera DIC problem. The geometry of the sample is measured in the calibration phase of DIC, but hardly used to correct the shape of numerical models which, most of the time, is considered perfectly flat whereas the sample is not.

Use of the mechanical knowledge (e.g. local elasticity or equilibrium) required reliance on an FE model. The integration of the regularization model into the DIC problem was only possible because the DIC problem was completely reformulated using finite elements instead of low-order polynomial independent subsets. This choice avoided difficult and error-prone re-projections. Most importantly, the classical stereo problem consists of a series of optimization problems - three for one time step - where the displacement is obtained in a post-processing stage. Under these conditions, it was very difficult - if not impossible - to apply mechanical regularization to the displacement, since it was not the primary unknown of the problem.

Finally, in its classical formulation, DIC lent itself less easily to assimilating multimodal measurements. The framework developed was thought to be capable of coupling different sources of data, such as infrared thermal cameras and also acoustic cameras, easily. To overcome these limitations, it was decided to write the DIC problem in the coordinate system of the part, with the displacement u(x) as the single unknown of a unique optimization problem [26, 27]:

$$u(x) = argmin \sum_c \int_\Omega [f_c \circ P_c(x) - g_c \circ P_c(x + u(x))]^2 dx$$

where f and g are the reference state and deformed state images of camera c. Mapping Pc is the camera model that maps the coordinates of a 3D point in the part coordinate system to a point in the image. The displacement is sought to minimize a functional that integrates the

camera c residual $r_c(x) = f_c \circ P_c(x) - g_c \circ P_c(x + u(x))$ over the domain and sums the contributions of all cameras. The camera models are classical for DIC. They consist of a set of intrinsic parameters p_{int} (focal length, image center, distorsions) and extrinsic parameters p_{ext} (rotations and translations of the camera w.r.t. a physical coordinate system). The intrinsic parameters are estimated prior to the analysis in a so-called calibration phase, similar to that of classic DIC, using calibration targets. Only the estimation of the initial shape s(x) and of the extrinsic parameters p_{ext} differ, as they are sought to minimize a functional very similar to the displacement one, but with a double sum on the cameras:

$$s(x), p_{ext} = argmin \sum_k \sum_c \int_\Omega [f_c \circ P_c(x + s(x)) - f_k \circ P_k(x + s(x))]^2 dx$$

Up to now, both shape s(x) and displacement u(x) fields belong to an infinite dimensional space, which is incompatible with computer resolution. Instead of considering subset-wise low order polynomials, in a subset based DIC, the chosen approximation space is sought here as a linear combination of FE Lagrange polynomials associated with an FE mesh, just like a finite element approximation subspace. The minimization of these nonlinear functionals is obtained using a Gauss-Newton algorithm, as the corresponding Hessians have a semi-analytic expression, which is computationally efficient. Since DIC is an ill-posed problem in the sense of Hadamar, regularization is a necessity. The classical way to regularize DIC is to play with the subset or element size as, the larger the subset, the higher the regularization. When large subsets are considered with low order polynomial approximations, it becomes difficult to accurately represent short varying solutions. In other words, the problem with this approach is that it leads to a trade-off between regularization (which would tend to increase the size) and approximation error (which would tend to decrease the subset). There are two families of alternative regularization techniques that do not have these limitations:

Strong regularization: this consists in considering a smaller, more regular approximation subspace. We call it strong because the solution is forced to belong strictly to this subspace.

The consequence is that the user has to trust the validity of this subspace because, if the actual solution does not belong to it, this will lead to a wrong solution. In a sense, we think that classical regularization (i.e. playing with the subset/element size) belongs to this first class. This class is sometimes called integrated DIC.

Weak regularization: this consists in keeping the same approximation subspace and in modifying the functional by adding a penalization term, in the spirit of Tikhonov's method. This penalty term is a measure of the irregularity of the displacement:

$$u(x) = argmin \sum_c \int_\Omega [f_c \circ P_c(x) - g_c \circ P_c(x + u(x))]^2 dx + \alpha ||u(x)||^2$$

where α is a penalty term that is a parameter of the method. It can be assimilated to a cut-off frequency of the low-pass filter. In other words, this method can be interpreted as a hybrid approach where the low frequency part of the displacement is driven by the gray level functional only (classical DIC) and the high frequency oscillations are driven strictly by both terms, as if we were dealing with a strong regularization.

As mentioned above, the main advantage of such a formulation is that it transforms the classical multiple optimization problems (2 stereo matches and 2 triangulations) of stereo DIC into a single optimization problem where the unknown is the displacement. It is therefore possible to prescribe both types of extended regularizations in a straightforward manner. To complement the partial displacement measurements of the vertex experiments (only the top of the specimen was visible), a strong regularization was performed. More specifically, it was possible to estimate the mechanical flows (forces and moments) at the boundaries of the specimen, considering a trustworthy mechanical model. An FE model was then assembled and the appropriate stiffness operator was used to construct a relevant reduced basis, L, dedicated to the boundary condition estimation:

$$u = L\,u_b \qquad \text{with} \qquad L^T = \left[-K_{ii}^{-1} K_{ib}\,;\, K_{bb}\right]$$

The problem is solved by projection onto this reduced basis, so that the displacement u is replaced by a reduced set of degrees of freedom u_b corresponding to the boundary nodes. The index b refers to boundary nodes, whereas i corresponds to interior nodes. By virtue of the Saint-Venant principle, formulated in this way, the problem is still ill-posed, since any resultant-free boundary fluctuation has little effect on the overall kinematics of the sample. Therefore, a weak regularization based on the gradient of the boundary displacement was added to limit short varying oscillations without having any great effect on the solution. For further details, the interested reader is referred to [35]. A first linear elastic model was used in a region close to the boundaries - far enough from the damage - to estimate the boundary conditions [5, 26]. Due to the rather large buckling that occurred, e.g. in shear, the accurate estimation of the mechanical fluxes in the post-buckling regime required a switch to a geometrically non-linear regularization. This required an updated stiffness matrix and reduced basis to account for the post-buckling stiffness drop. The method not only outperformed the classical DIC + classical flux estimation technique in terms of accuracy and uncertainties, but also allowed us to estimate the strain on the hidden face with spectacular accuracy compared to strain gauges, see Figure 11. Figure 12 demonstrates the importance of the model in the measurement process. The displacement extracted from a linear regularization is indeed inadequate. Performing a nonlinear regularization improves the estimation of the displacement fields obtained. When the number of cameras in a multiview setting increases, the calibration may become costly, since the number of terms in the double sum is n(n+1)/2 with n cameras. An alternative approach consists in building a reference texture denoted f [27]. Then the functional becomes:

$$s(x), p_{ext} = argmin \sum_c \int_\Omega \left[f_c \circ P_c(x + s(x)) - f(x)\right]^2 dx$$

3.3 Coupled Thermal/Kinematic Measurement

The damage-generated heat source is precious information for estimating and validating the damage models of composite materials. In the context of large buckling, the samples were subject to significant out-of-plane displacements and rotations, which transported the temperature field in the IR camera. In other words, the IR camera recorded the temperature in a kind of Eulerian vision of the movement, whereas the numerical FE models were formulated in a Lagrangian setting. As stated above, with the data assimilation formalism described earlier, coupling multimodal data is convenient [28]. For instance, it was possible to correct the temperature field by using the measured kinematic field. In practice, the proposed framework allowed us to bring all raw data from multimodal images to the finite element mesh of the sample using dedicated calibrated camera models. An additional IR camera model P_{th} was calibrated as illustrated in Figure 13. In this way, for any point x in the sample coordinate system, it was possible to obtain the Lagragian temperature Ti value by simply evaluating the IR image t(x) at the advected solution position:

$$T_x = t \circ P_{th}(x + u(x))$$

where u(x) is the displacement field measured prior to the thermal estimation. This operator is direct and cost-free, since everything is known. An example of a reconstructed Lagrangian temperature field is plotted in Figure 14. It is worth mentioning that visible and infrared cameras must be synchronized. If this is not done with hardware, it is still possible to perform a post-synchronization by performing rigid body DIC on the jaws of the testing machine for both image sets. Most of the experiments performed on the VERTEX machine involve an IR camera observing the painted side of the sample. Several thermography problems thus arise when trying to quantify the thermal state in the experiment. The emissivity of the surface is far from homogeneous, due to different colors being used. The geometry of the sample is changing (bending, buckling), which modifies the relative orientation of the camera with respect to the surface normal and thus the measurement. The coupling of kinematic and

thermal measurements can improve the measurements by taking such phenomena into consideration.

3.5 Multiscale Measurement

Whilst the use of stereo DIC has been described in detail previously, the focus of the preliminary section was to establish the boundary conditions and therefore observations were made on a macro scale. The overall behavior of the plate is not the only quantity of interest in this study, as the crack evolution is also of utmost interest and the kinematics of the (notched) central part of the specimen provides a great deal of information for characterization. Therefore, several zones need to be monitored at different resolutions. The arrangement of the cameras (far field, near field and texture) is shown in Figure 15. In order to calibrate the full stereo vision rigs (3 pairs of cameras) within the FE-DIC framework, the intrinsic and extrinsic parameters of all cameras must be determined in a global reference coordinate system. For this purpose, the calibration is performed in several steps and relies on the use of a reference "texture" with high resolution cameras (29 MPx) as shown in Figure 16. The intrinsic parameters of the cameras are obtained using suitable calibration targets. For the large field of view ("Texture" and "FF"), a target of 12x12 23-mm dots is used, while a smaller one (12x9 5-mm dots) is used for the NF cameras. The extrinsic parameters of the high-resolution cameras are then calculated using a DIC-based calibration method that also measures the actual shape of the plate. This algorithm is initialized with 6 points corresponding to recognizable features on the plate (notches, holes, line intersections, etc.). A similar algorithm is then used to calibrate the FF and NF cameras, but the initial features used for initialization are automatically detected within the speckle and correlated with the high-resolution images.

Once the position of the cameras has been initialized, a global minimization of the DIC function proposed in Figure 16 is performed. Once this calibration has been carried out, a

global stereo-FEDIC function can be minimized using the same method as described above. Each stereo system (NF and FF) will provide data depending on the visibility of the object and more (and finer) information will be available around the notch, as can be seen in Fig.17. It is clear that the quality of the displacement around the notch is greatly improved by the use of NF cameras. It should be noted that, while most of the processing is automated, the overall analysis still requires several hours (not including testing, which can also be lengthy). The computational efficiency aspect of the methods is another topic of interest that could be improved and developed.

At the beginning of the adventure, we made the speckles in a very traditional way, using simple cans of paint. It was a tricky operation. The operator had to get finer patterns at the tip of the notch (to enable near-field measurement). We soon turned to printing optimized patterns for each scale directly onto the specimen [5, 26]. This resulted in the nesting of 2 fine patterns in a gossamer pattern. While this approach allowed us to obtain very high-resolution measurements at each scale in the corresponding part of the speckle, it made it difficult to relate the near-field and far-field cameras (relative calibration). We looked for alternatives. We could have chosen to use the two-scaled chessboard suggested by Bomarito et al. [29], but finally decided to use a 'fractal' speckle pattern (see Fig. 2) proposed by Fouque et al. [30], which presents the advantage of not having to prioritize the scales of the view/speckle. This type of speckle makes it possible to maintain a gray level gradient across multiple resolutions, thus simplifying initialization (in a classic coarse-to-fine approach) and simplifying the matching of multi-scale images.

3.6 Discussion

As mentioned earlier, one ambition would be to use DIC based measurements for real-time machine control. It is, for instance, particularly tempting to be able to fully control an envelope-type load by using the images collected during the test. This would need image

processing to be speeded up enormously: from the several minutes currently required for a load state to nearly one second. The challenge is tremendous. Subset DIC formulations lead to a set of small independent problems, one for each subset, which makes the technique well suited for an efficient parallel implementation. Finite Element approaches to DIC lead to one large problem, for which an efficient parallel implementation is less direct. High performance computing implementations [31, 32] or reduced approximations are therefore needed to estimate the load applied and also to monitor the deformation of the specimen in "real time" [33-34]. Grotto et al. [6] show that, by taking the whole machine into account in the simulation, the observed buckling modes can be reproduced much better. One idea could therefore be to use this model of the machine to propose the next load increment to be applied to the actuators. It then seems essential to recalibrate, even roughly, the behavior of the machine as a function of images/measurements taken at different scales. In addition, it may be interesting to use the FE DIC stereo measurements to identify parts of the model, either on the elastic part (e.g. to better describe the difference in fiber direction tension/compression behavior), or even for specific parts of the model in the non-linear domain [36, 37]. A number of questions remain open if such approaches are to be applied to large-scale structures, finite strain, large displacements/rotations or if the lighting conditions are difficult to manage. Recently, a Photometric-DIC (PhDIC) was proposed to avoid problems like specular reflection and visibility issues [38]. An extension of this approach to structural scale experiments would improve both quantitative kinematic and thermal monitoring.

4. Case Study 1: Notched Plates.

Today, the structures of civil passenger aircraft must be certified as having demonstrated their ability to withstand an exceptional event, such as an uncontained engine explosion, which can create significant damage to a fuselage (see Figure 18 (a)). Such an in-flight incident can generate a large notch in the fuselage, which may be contained in a bay (skin alone between

stringers and frames) or may cut through a stiffening member (frame or stiffener). Most of the time, the sizing of a fuselage according to this criterion is performed with a very expensive test at scale one (see Figure 18 (c)). On the other hand, the residual strength in presence of crack damage of CFRP structures is generally evaluated through the point-stress or similar methods in open-hole tests [39-44], in which the holes are sometimes also referred to as "notches". The size effect of the hole size relatively to the sample width is widely documented in the literature but mostly focuses on small circular holes with diameters up to 50 mm. Other publications deal with sharp notches [45, 46] which are more critical for large damage [47, 48]. The point-stress method is used as a simple criterion to evaluate a preliminary damage state at panel level (referred to as stable damage state). Nevertheless, the d_0 criterion distance value depends on numerous parameters, such as layup, ply thickness, and material. It might not be representative of larger crack phenomenology as it is usually identified with coupon tests. In notch tests, coupons tend to fail directly and catastrophically, whereas, in larger samples, the crack propagates more progressively. Therefore, the VERTEX system provides boundary conditions and multiaxial loadings which are closer to the real structures but at lower cost compared to full scale tests as in Figure 18(c). A typical VERTEX specimen (see Figure 19) was milled to create a 100 mm center-notch to keep the ratio W/L = 4 and to maintain representativeness of large damage phenomenology. The notch was machined with a 2 mm mill. This process left an end notch radius of 1 mm. Unidirectional fibers and thermoset or thermoplastic resin were used in prepeg form. For confidentiality reasons, the exact material reference, the material properties, the thickness and the manufacturing processes of some of the materials used cannot be disclosed in this article. First, the influence of the stacking sequence was studied with prepegs made of Hexcel's T700-M21 carbon epoxy unidirectional laminate with a nominal thickness of 0.125 mm. Two specimens were also manufactured with a double thickness ply of 0.250 mm. Three symmetrical stacking

sequences of 13 plies were studied. The three different stackings (C3-1, C3-2, C3-3) presented the same number of plies in each direction (0, 90 and ±45), and only the relative position of the plies changed between layups. X's are used to avoid disclosing the orientations of some plies:

– C3-1 [45/45/X/X/X/90/0/90/X/X/X/45/45]

– C3-2 [X/X/X/X/0/90/0/90/0/X/X/X/X]

– C3-3 [X/X/X/X/X/0/0/0/X/X/X/X/X]

Stress/strain curves obtained in tension using the methodology explained in the previous section are shown in Figure 20. The vertical arrows represent the final failure of the laminates, corresponding to cuts that propagated to the edges of the test piece. Using the in-situ measurement, linear curves were obtained until the damage occurred. In this way, the phases of initial positioning and the possible non-linearities of the assembly were filtered. The specimens were of the same stiffness, 38 GPa, close to the 43 GPa determined experimentally on a notched coupon [47, 48]. This decrease in stiffness was due to the ratio of notch width to specimen width, which was higher for VERTEX (1/4) specimens than for coupon-scale (1/6) specimens. Localized bending was observed near the notch (Figure , Layout C3-1). It accelerated the propagation of the crack and thus reduced the maximum failure stress. F points correspond to a maximum deflection of the notch border approximately equal to the thickness of the laminate (single thickness: 1.625 mm). The same reference (1.625 mm) was used (in value) for laminates C3-1d. This double thickness laminate, being stiffer in bending, required a higher load to reach a similar deflection. The failure stress observed for the double thickness specimen was therefore greater than those observed for the ‘‘single thickness”. The C3-3 specimen showed higher resistance to damage propagation and the failure stress of C3-1, double sized version, was increased even more. Both stacking sequence and thickness effect were therefore identified. C3-1, C3-2 and C3-3 were also tested in shear and

tension+shear. In both tests (Figure 21 and Figure 22), the C3-3 stacking sequence exhibited higher failure stress and dissipated more energy before total failure. More recently, the influence of pressure on tensile, shear and combined tension+shear tests has been investigated (Figure 23 and [66]). Additional pressure seems to have a slight influence, mainly on the appearance of the first fiber failure detected with an Infrared Camera.

5. Case study 2: Testing of Impacted Plates

CFRP composite structures are particularly vulnerable to low energy impacts. This leads to a policy of impact damage tolerance and sizing which in turn leads to overweight. These low energy impacts, for example due to unexpectedly dropping of tools [49, 50], can occur in service, during ground operations or in aircraft manufacturing. Even if the damage due to impact is not detectable by visual inspection, the residual resistance of the composite structure can decrease by more than 50% [51-53]. The most critical loading case acting on a real aeronautical structure is compression loading, so experimental tests are performed on small coupons of size 100×150 mm^2 in order to certify and size the aeronautical composite structures. Past experience has shown that the allowable values determined by this methodology are conservative [18, 19, 50, 54, 55]. Thus, in order to be less detrimental and to be more representative of the real life of the composite structure, the loss of residual strength after impact should be evaluated at the level of the structural element. This is one of the main advantages of the Vertex test bench. Therefore, an experimental study was performed with the Vertex machine in order to evaluate the loss of residual strength after impact of composite panels with a size more representative of the structural element level [5, 56]. For this size of panel, the important points are the boundary conditions and the postbuckling. Contrary to the situation observed with classical coupons of 100×150 mm^2, where the postbuckling is almost non-existent (which is logical because the objective is to evaluate the loss of residual strength on the allowable in compression), considerable postbuckling developed during the structural-

element-level test: consequently, the residual strength was clearly less influenced by the impact; this result was clearly highlighted during this study [57, 58], where a unidirectional carbon/epoxy prepreg T700/M21, with a 0.25 mm-thick ply was used. The 14 ply laminate was manufactured with the stacking sequence $[45_2/\text{-}45_2/0_2/90]_S$, giving a total thickness of 3.5 mm. Eight specimens were manufactured and tested as mentioned in Table 1: seven were impacted while one was kept unimpacted in order to compare the loss of residual strength, and each underwent a different loading path in the VERTEX test rig.

Impact tests were performed with the gas launcher of the Clement Ader Institute impact platform [59] at velocities between 54 and 110 m/s, with a spherical steel impactor 19 mm in diameter and weighing 28 g, which led to impact energies between 40 and 170 J (Table 1). During the impact, the composite panels of 538×400 mm^2 size were simply supported by a 400×400 mm^2 impact window (Figure 24, left). A high-speed camera and a speckled pattern painted on the ball made it possible to evaluate the impactor displacement, velocity and acceleration [60], and thus the impact force. Of course, the higher the energy of the impact, the greater are the maximum displacement and the impact force. Then C-scan investigation was performed on each panel in order to evaluate the delaminated area. Logically, the most delaminated interface was the first interface situated on the non-impacted side, the -45°/45° interface (Figure 24, right). It should be noted that, compared to classical impact on a small coupon, the extent of the delamination was greater due to the size of the panels and to the significant impact energy levels. This point is interesting because, despite the size of these delaminated areas, it was shown that the loss of residual strength was relatively small, due to the marked post-buckling that developed during the experiments and the hyperstatic clamping of the sample. Then the 8 panels were tested with different loading cases (Table 1), the stress curves for which (σ_{xx}, τ_{xy}) are plotted in Figure 25 using the methodology presented in Section 3. This graph also shows the buckling and the failure. It should be noted that, due to

problems of stress concentration in the corners of the plates, most of the final failure started in a corner and propagated in the middle of the plate, at the impact point.

In order to better understand the progression of the experiment, the stress-strain curves of the specimens C, F and H are plotted in Figure 25 and the final failure of specimen F is drawn in Figure 26. The non-impacted specimen, H, specimen C impacted at 75 m/s and specimen F impacted at 100 m/s (Table 1) were loaded using the torsion actuators 3 and 4, leading to a tension/shear loading path (Figure 25). This coupling was partly due to the Vertex machine and partly due to the classical tension loading resulting from a shear post-buckling. At the beginning of the test, the stiffnesses of the 3 specimens were similar to one another and similar to the theoretical values. The buckling point logically occurred later for the non-impacted specimen than for impacted specimens and a different loading path was observed for the impacted specimens. It should be noted that, due to the particular concept of the Vertex machine, even if the displacement imposed on the machine is the same, the loading path also depends on the specimen. So, with the same imposed displacement for these 3 samples, the loading paths were slightly different. The buckling shapes for the 3 samples are similar, with three half waves (Figure), and the final failures are also similar, with the fiber failure of the 45° ply situated on the impacted side and its propagation along the diagonal direction. It is difficult to evaluate the initiation of the final failure because of its high speed (despite the use of the infrared camera) but it seems to have initiated at the bottom right corner of the panel (Figure c). In the first image where the failure is observed (Figure c), then one millisecond before the second image (Figure d; the frame rate of the infrared camera is 1 kHz), the crack has not yet reached the top left corner. Analyzing each loading case individually was crucial for understanding the behavior of each specimen under varying loading conditions. In Figure 25, we can observe all the loading paths of the specimens along with their corresponding buckling points on a (σ_{xx}, τ_{xy}) graph. It is worth noting that, given the differences in the

energy levels at which specimens were impacted, it was not feasible to plot envelope curves for the various impact energy levels [57]. As expected, the compression and compression/shear loading paths emerged as the most critical factors affecting the structure's integrity. In contrast, the tension and tension/shear loading paths tended to mitigate damage propagation. Interestingly, when comparing specimens subjected to the same loading path but impacted at different energy levels (e.g., specimens E and G in pure compression and specimen C in tension/shear), it appeared that the impact damage had minimal influence on the occurrence of buckling but played a significant role in determining the eventual failure. For specimen H, which was not impacted but subjected to the same loading path as specimens C and F, buckling and final failure occurred later in the testing process.

Drawing direct conclusions about the effect of the impact on Vertex tests can be challenging, given that the loading path is intricately tied to the damage state of the structure. Typically, impacts can affect the residual strength, with greater impact damage leading to reduced residual strength. Additionally, impacts can influence the loading path itself, and these two phenomena are interconnected. To better distinguish between these effects, a simplified elastic Finite Element Model (FEM) of the Vertex plate was constructed [58]. This model utilized boundary conditions derived from DIC (Digital Image Correlation) data, as explained in the subsection 3.2, to replicate the loading path. Various tests conducted on the VERTEX test rig were then simulated using this simplified model, and the numerical results are presented in Figure 28. In this figure, the black lines represent the experimental results, while the colored lines depict the finite element results. The correlation between the numerical and experimental loading paths is notably strong. The behaviors are closely aligned until buckling occurs. It is important to note that the differences observed after buckling may be attributed to the simplicity of the model, which does not account for composite damage factors such as

fiber failure, delamination, or matrix cracking. Nonetheless, comparing the experimental buckling points with the numerical results yields valuable insights into the structural response.

The results obtained indicate that, up to the point of buckling, the impact energy level exerts minimal influence on the specimens. However, an interesting observation is made with the non-impacted specimen H, where buckling occurs later than in specimens subjected to the same loading path. Subsequent to buckling, a noticeable delay is observed in various phenomena (such as mode jump in pure compression loading, initial and final failure) in the most damaged plates. Nevertheless, it appears that the final failure originates from the impact point solely in the pure shear test. In compression, it seems that the impact damage has no discernible effect on the final failure path, which initiates in the bolted zone at the bottom left corner of the specimen. In the cases of compression/shear and tensile/shear loading, thermal camera images suggest that the final failure initiates in the bottom left corner but is guided by the impact point to propagate along the diagonal of the specimen. Exploring more specimens under compression loading, particularly non-impacted ones, could provide valuable insights into the scale effect on compression after impact. Nevertheless, these initial findings underscore the complexity of the structural response at the scale of an impacted plate, as compared to coupon specimens. Additionally, they highlight the significance of impact location, and it is noteworthy that the current allowances used to size aerospace composite structures may be overly conservative. As elucidated in this paper, one of the main challenges in employing such a test rig is to identify the boundary conditions that affect the specimen. The development and validation of a simplified model for transferring boundary conditions from DIC to Abaqus is a crucial step in enabling the "Virtual Testing" approach to be effectively applied.

6. Case study 3: Wrinkling in sandwich structures

Sandwich structures are widely used in light aviation and helicopters [53]. To reduce weight and to lower fuel consumption as far as possible, very thin skins and very light cores are used. However, the design of these sandwich structures is delicate, in particular because of local buckling, also commonly called “wrinkling”. This phenomenon can only be captured by refined 3D models and the available analytical formulas prove to be imprecise and are only given in compression [61]. Furthermore, the allowable values are obtained from coupon tests, which are also difficult to implement and can present experimental biases, as highlighted in a publication by Hoff and Mautner in 1948 [62]. In this context, local buckling tests were conducted on specimens representative of the technology of one manufacturer, Elixir Aircraft, in compression and shear. Using the properties of asymmetrical sandwich structures [17, 18], the specimens were sized so that the buckling took place on the visible side. The areas where the forces were introduced were reinforced by additional layers and by cores with a density greater than that of the area of interest. Five plates were manufactured with the stacking described in Table 2 and the faces of interest are described in Figure 29. Note that, for the specimen F51_D2, tested under compressive load, a 60 mm wide strip of 2 × unidirectional 0° ply was added (blue area in Fig. 29). The tests were monitored with a high-speed camera, a thermal camera, and near- and far-field image correlation. The rupture mode observed was quasi-explosive but, thanks to the instrumentation deployed, the rupture scenario could be identified and shown to be indeed local buckling. Image correlation made it possible to analyze the progressive appearance of the waves but the break and, in particular, its location could only be captured using the high-speed camera together with the thermal camera. The compressive and shear failure scenarios are shown in Figure 30. It should also be noted that, for the specimens with a Nomex nida core, the rupture occurred in the zone where the forces were introduced and no buckling could be observed. It is interesting to note that, for specimen F51 D2 with reinforcement folds in the center, a local buckling failure still occurred in the

reinforcement although the thickness was locally greater there. This can be explained by the fact that the area, being more rigid, “drains” the compressive forces and is more loaded than the adjacent skin. This study demonstrated the feasibility of local structural buckling tests [63]. A rich test/computation dialog was also set up but will not be developed here [64].

7. Envelope curves (non-proportional tests)

The validation of a loading domain, and thus the integrity of the structure to be sized, generally requires many tests because the domain is usually explored with proportional loadings. Serra et al. [5] initially swept the tension-shear domain of loading with envelopes of increasing amplitudes, introducing a safety assessment of the loading domain between the proportional loadings tested previously. The definitions of the envelope tests were based on the results obtained in the proportional tests (Figure 31). This first step was to validate the concept of a safe envelope. In [65], the Safe Life Domain method is formalized and studied in greater depth to validate a whole domain of loading of a given sample, with single envelope testing based on prior simulations and thanks to the VERTEX multi-directional test rig. Figure 32 illustrates the Safe Life Domain method. Numerical simulations are performed to explore the domain of loading and locate failures – basically by using a failure point for each simulation of proportional loading. The failure points delineate a critical border, which is the frontier between the safe domain and the failed domain. The numerical model presented in Section 2 and [6] is used. A safety margin is taken from the critical border, and a single envelope test is performed along the critical border (Figure 32). *At the end of this envelope test, if the sample is actually safe (no failure detected), then the whole domain of loading encircled is considered safe.*

The critical border shape depends on:

- The design (flat panel, stiffened panel, sandwich, assembly)

- The material, notably the stacking sequence of a given laminated composite
- The material failure criterion (Yamada-Sun, maximum fiber strain, first fiber failure, etc.)
- The damage type (pristine sample, 100 mm notch, loading after impact, etc.)
- The load shape (pure tension, VERTEX's tension, actual in-situ tension): see previous study for an introduction to the severity and representativeness of loading shapes.

Ultimately, stacked plots of the critical borders of various cases is a matter of great interest for the aeronautical industrial wishing to size structural elements, especially generic panels. Figure 33 illustrates nomograms of critical envelopes that could be used to choose materials during the sizing process, depending on the typical load cases to be withstood. Envelopes are determined in a homothetic manner from the critical border (Figure 34). Figure displays the envelope test, the proportional tests, and the simulated critical envelope. The initial pressure applied an initial bias of tension on the further loading. The envelope $k = 1.0$ of $T_{envelope}^{pres}$ fits the numerical simulation of the same jack setpoints perfectly, except for the shear portion (low tension) where the backlash take-ups again alter the numerical prediction of the machine stiffness. Figure highlights the largest envelope completed without failure. This is considered as the safe life domain.

8. Conclusions

The VERTEX test bench has demonstrated its capacity and usefulness for testing aeronautical structures, both for light aviation and for large aircraft manufacturers. Large notches, impact and wrinkling of sandwich structures have been presented, whereas ongoing studies have not: postbuckling of impacted single-stiffened structures [20], thermoplastic specimen with large notches and buckling of wood based-sandwich structures. Phenomena and rupture scenarios

are different from those of overly simplistic and conservative coupon tests. The complexity is greater, with postbuckling coupled with fracture most of the time, but the phenomena observed are closer to reality and demonstrate that the coupon tests are too conservative, in particular for compression after impact and large notches. The tests are generally highly monitored and specific DIC approaches have been developed to capture the fluxes inside the specimen and even the strains and stress on the hidden faces. This approach also enables an efficient experiment/computation dialog. The possibility of exploring a large area of loading and the validation by a single path through "envelope tests" has also been demonstrated. Today, the test is still on the research side and many efforts are still to be made before it can become a test certified by the aviation authorities.

9. Acknowledgments

These ten years of research are the result of two main funding sources. The first one was the VERTEX Project, funded by the French National Research Agency under the MATETPRO program (ANR – 12 – RMNP-0001). The second main result, the VIRTUOSE program (VIRTUal testing of aerOnautical StructurEs) was funded by the "Fondation Jean-Jacques et Felicia Lopez-Loreta pour l'Excellence Académique". The authors also wish to thank the industrial partners who supported the research through the previous funding or direct collaboration: Airbus, Elixir Aircraft, Segula Ingénieurie and Avions Mauboussin.

10. References

[1] Rouchon J. Certification of Large Airplane Composite Structures, Recent Progress and New Trends in Compliance Philosophy. Proceedings of ICAS 2 (1990), pp. 1439-1447
[2] Leon-Dufour J-L. Dimensionnement des structures composites aux dommages. Presented at the Journée 3AF, CNES, Toulouse, 2008.
[3] US department of Defense. Composite Material Handbook. US-mil Hbk 17
[4] Tenney DR, Davis JG, Johnston NJ, Byron Pipes R, McGuire JF. Structural Framework for Flight: NASA's Role in Development of Advanced Composite Materials for Aircraft

and Space Structures. NASA/CR–2011-217076 (https://ntrs.nasa.gov/citations/20110012179.
[5] Serra J, Pierré JE, Passieux JC, Périé JN, Bouvet C, Castanié B. Validation and Modeling of Aeronautical Composite Structures Subjected to Combined Loadings: the VERTEX Project. Part 1: Experimental Setup, FE-DIC Instrumentation and Procedures. Comp Struct 2017;179: 224-244
[6] Grotto F, Peta O, Bouvet C, Castanié B, Serra J. Testing structural elements under multiaxial loading: a numerical model of the bench to understand and predict complex boundary conditions. Aerospace 2024, 11(1), 68 https://doi.org/10.3390/aerospace11010068.
[7]https://www.youtube.com/watch?v=kccruUS9Hg4&ab_channel=BristolCompositesInstitute
[8] https://www.composites-certest.com/research-challenge-3/
[9] https://www.irt-jules-verne.fr/equipements-de-pointe/banc-dessai-multiaxial/
[10] Bakuckas JG et al. Assessment of emerging metallic structures technologies through test and analysis of fuselage structure. SN Appl. Sci. 2019;1: 1521.
[11] Wolf K, Kossira H. An Efficient Test Method for the Experimental Investigation of the Post-buckling Behavior of Curved Shear Panels. ECCM Composite Testing and Standardization, Amsterdam (1992)
[12] Romeo G, Frulla G. Buckling and Post-buckling Behavior of Anisotropic Plates Under Combined Biaxial Compression and Shear Loads. ECCM Composite Testing and Standardization, Amsterdam (1992)
[13] Peters RW. Buckling tests of flat rectangular plates under combined shear and longitudinal compression. NACA Technical Note, 1750 (1948)
[14] Klein H, General About Buckling Tests With Thin-walled Shells, Rapport DLR- Mitt, 89–13.
[15] Lightfood MC, Ambur DR. Open Architecture data System for NASA Langley Combined Loads Test System. AIAA Paper AIAA-98-0345.
[16] Rouse M, Young RD. Design and evaluation of composite fuselage panels subjected to combined loading conditions. J. Aircraft 2005;42 (4):1037-1045.
[17] Castanié B, Barrau JJ, Jaouen JP. Theoretical and experimental analysis of asymmetric sandwich structures. Comp Struct 2002;55(3):295–306.
[18] Castanié B, Barrau JJ, Jaouen JP, Rivallant S. Combined shear/compression structural testing of asymmetric sandwich structures. Exp Mech 2004;44(5):461–472.
[19] Castanié B, Bouvet C, Aminanda, Y, Barrau JJ, Thevenet P. Modelling of low-energy/low-velocity impact on Nomex honeycomb sandwich structures with metallic skins. Int J Imp Eng 2008;35(7):620–634.
[20] Grotto F, Bouvet C, Castanié B, Serra J. Design and Testing of Impacted Stiffened CFRP Panels under Compression with the VERTEX Test Rig. Aerospace 2023;10(4):327.
[21] Tao G, Xia Z. A non-contact real-time strain measurement and control system for multiaxial cyclic/fatigue tests of polymer materials by digital image correlation method. Pol Test 2005;24(7):844-855.
[22] Fayolle X, Calloch S, Hild F. Controlling testing machines with digital image correlation. Exp Tech 2007 ;31(3) :57-63.
[23] Le Flohic J, Parpoil V, Bouissou S, Poncelet M, Leclerc H. A 3D displacement control by digital image correlation for the multiaxial testing of materials with a Stewart platform. Exp Mech 2014;54(5):817-828.
[24] Schreier H, Orteu J-J, Sutton MA. Image Correlation for Shape, Motion and Deformation Measurements Basic Concepts,Theory and Applications. Springer Eds, 2009

[25] Sztefek P, Olsson R. Tensile stiffness distribution in impacted composite laminates determined by an inverse method. Comp Part A 2008;39(8):1282-1293.
[26] Pierré JE, Passieux JC, Périé JN. Finite Element Stereo Digital Image Correlation: Framework and Mechanical Regularization. Exp Mech 2017;57(3):443-456.
[27] Dufour JE, Hild F, Roux S. Shape, displacement and mechanical properties from isogeometric multiview stereocorrelation. J Strain Anal Eng Des 2015;50(7):470-487.
[28] Charbal A, Dufour JE, Hild F, Poncelet M, Vincent L, Roux S. Hybrid stereocorrelation using infrared and visible light cameras. Exp Mech 2016;56:845-860.
[29] Bomarito GF, Hochhalter JD, Ruggles TJ, Cannon AH. Increasing accuracy and precision of digital image correlation through pattern optimization. Opt Las Eng 2017;91:73-85.
[30] Fouque R, Bouclier R, Passieux JC, Périé JN. Fractal Pattern for Multiscale Digital Image Correlation Exp Mech 2021;61:483–497.
[31] Passieux JC, Périé JN, Salaün M. A dual domain decomposition method for finite element digital image correlation. Int J Num Meth Eng 2015;102(10)1670-1682.
[32] Ronovsky A, Vasatova A. Elastic image registration based on domain decomposition with mesh adaptation. Adv Elec Electron Eng 2017;15(2):322-330.
[33] Durif E, Réthoré J, Combescure A, Fregonese M, Chaudet P. Controlling Stress Intensity Factors During a Fatigue Crack Propagation Using Digital Image Correlation and a Load Shedding Procedure. Exp Mech 2012;52:1021–1031.
[34] Carpiuc-Prisacari A, Poncelet M, Kazymyrenko K, Leclerc H, Hild, F. A complex mixed-mode crack propagation test performed with a 6-axis testing machine and full-field measurements. Eng Frac Mech 2017;176:1-22.
[35] Dufour JE, Colantonio G, Bouvet C, Périé JN, Passieux JC, Serra J. Monitoring structural scale composite specimens in a postbuckling regime: The integrated finite element stereo digital image correlation approach with geometrically non-linear regularization, Strain 2023;59(5):12450.
[36] Pottier T, Vacher P, Toussaint F, Louche H, Coudert T. Out-of-plane testing procedure for inverse identification purpose: application in sheet metal plasticity. Exp Mech 2012;52:951-963.
[37] Wang, Y., Coppieters, S., Lava, P., & Debruyne, D. (2016). Anisotropic yield surface identification of sheet metal through stereo finite element model updating. The Journal of Strain Analysis for Engineering Design, 51(8), 598-611.
[38] Fouque R, Bouclier R, Passieux JC, Périé JN. Photometric DIC: a unified framework for global Stereo Digital Image Correlation based on the construction of textured digital twins. J Theo Comp Appl Mech 2022;2:1-32.
[39] Awerbuch J, Madhukar MS. Notched strength of composite laminates: predictions and experiments—a review. J Reinf Plast Compos 1985;4(1):3-159.
[40] Bazant ZP. The scaling of structural strength. HPS, London (2002)
[41] Bazant ZP, Daniel IM, Li Z. Size effect and fracture characteristics of composite laminates. J Eng Mater Technol 1996;118 (3):317-324.
[42] Wisnom MR, Hallett SR, Soutis C. Scaling effects in notched composites. J Compos Mat 2010;44(2):195-210.
[43] Xu X, Wisnom MR, Mahadik Y, Hallett SR. An experimental investigation into size effects in quasi-isotropic carbon/epoxy laminates with sharp and blunt notches. Compos Sci Technol 2014;100:220-227.
[44] Camanho PP, Maimí P, Dávila CG. Prediction of size effects in notched laminates using continuum damage mechanics. Compos Sci Technol 2007;67(13):2715-272.
[45] Kamala Kannan V, Murali V, Rajadurai A, Nageswara RB. Failure assessment on central-sharp notched carbon/epoxy laminates. Mat Design 2010:31(9):4348-4355.

[46] Hochard C, Lahellec N, Bordreuil C. A ply scale non-local fibre rupture criterion for CFRP woven ply laminated structures. Comp Struct 2007;80(3):321-326.
[47] Serra J, Bouvet C, Castanié B, Petiot C. Experimental and numerical analysis of Carbon Fiber Reinforced Polymer notched coupons under tensile loading. Comp Struct 2017;(181):145–157.
[48] Serra J, Bouvet C, Castanié B, Petiot C. Scaling effect in notched composites: The Discrete Ply Model approach. Comp Struct 2016;148:127–143.
[49] Susainathan J, Eyma F, De Luycker D, Cantarel A, Bouvet C, Castanié B. Experimental investigation of compression and compression after impact of wood-based sandwich structures. Comp Struct 2019;220:236-249.
[50] Abrate S, Castanié B, Rajapakse YDS. Dynamic failure of composite and sandwich structures. Springer, 2013
[51] Chang JB, Goyal VK, Klug JC, Rome JI. Composite Structures Damage Tolerance Analysis Methodologies. NASA/CR-2012-217347.
[52] Tropis A, Thomas M, Bounie JL, Lafon P. Certification of the composite outer wing of the ATR72. J of Aeros Eng, Proc Inst Mechl Eng Part G 1994;209: 327-339.
[53] Castanié B, Bouvet C, Ginot M. Review of composite sandwich structure in aeronautic applications. Comp Part C 2020;1:100004.
[54] ASTM D7136/D7136M. Standard Test Method for Measuring the Damage Resistance of a Fiber-Reinforced Polymer Matrix Composite to a Drop-Weight Impact Event, 2015
[55] Rivallant S, Bouvet C, Abdallah EA, Broll B, Barrau JJ. Experimental analysis of CFRP laminates subjected to compression after impact: The role of impact-induced cracks in failure. Comp Struct 2014:111;147-157.
[56] Serra J, Pierré JE, Passieux JC, Périé JN, Bouvet C, Castanié B., Petiot C. Validation of aeronautical composite structures under multiaxial loading: the VERTEX Project. Part 2: Load envelopes for the assessment of panels with large notches. Composite structures, 180 : 550-567, 2017
[57] Trellu A, Pichon G, Bouvet C, Rivallant S, Castanié B, Serra J, Ratsifandrihana L. Combined Loadings After Medium Velocity Impact on Large CFRP Laminate Plates: Tests and enhanced computation/testing dialogue. Com Sci Tech 2020;196:108194.
[58] Serra J, Trellu A, Bouvet C, Rivallant S, Castanié B, Serra J, Ratsifandrihana L. Combined loadings after medium velocity impact on large CFRP laminated plates: Discrete ply model simulations. Comp Part C 2021;6:100203.
[59] STIMPACT Platform, http://www.institut-clement-ader.org/plateformes/stimpact/
[60] Passieux JC, Navarro P, Périé JN, Marguet S, Ferrero JF. A Digital Image Correlation Method For Tracking Planar Motions Of Rigid Spheres: Application To Medium Velocity Impacts. Exp Mech 2014:54;1453-1466.
[61] Ginot M, D'Ottavio M, Polit O, Bouvet C, Castanié B. Benchmark of wrinkling formulae and methods for pre-sizing of aircraft lightweight sandwich structures. Composite Structures, 2021;273:114387.
[62] Hoff NJ, Mautner SE. The buckling of sandwich type model. J Aeronaut Sci 1945:12.
[63] Ginot M, Bouvet C, Castanié B, Serra J, Mahuet N. Local buckling on large sandwich panels used in light aviation: Experimental setup and failure scenarios. Comp Struct 2023;304:116439.
[64] Ginot M, Bouvet C, Castanié B, Serra J, D'Ottavio M, Mahuet N. Local buckling on large sandwich panels applied to light aviation: Experimental and computation dialogue. International Journal of Solids and Structures 2023;268:112170.
[65] Grotto F. Contribution à l'étude des structures composites endommagées sous sollicitations multiaxiales et enveloppes de charge. PhD University of Toulouse. https://www.theses.fr/s258129

[66] Grotto F, Bouvet C, Castanié B, Serra J. Experimental behaviour of aeronautical notched carbon fibre reinforced thermoplastic panels under combined tension-shear-pressure loadings. Eng Fail Anal 2023;146,107075.

11. Figures

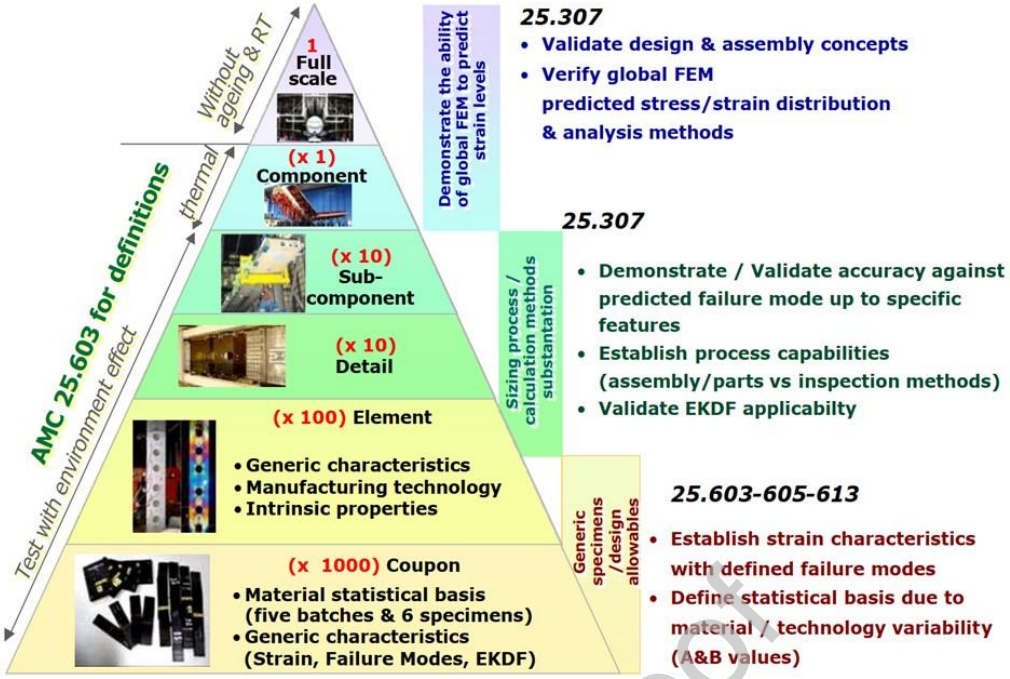

Figure 1: The pyramid of tests [1] representing the numerous small mechanical tests providing a design basis for fewer and larger tests [2] (Courtesy of Airbus).

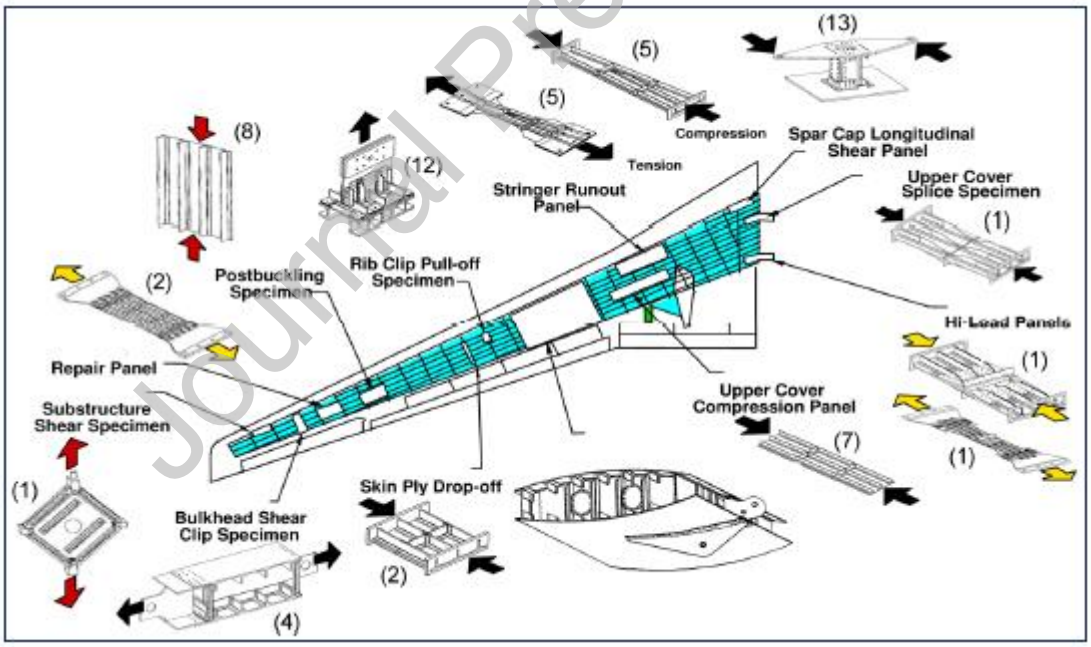

Figure 2: Validation of tests of a carbon wing box by NASA [4] (Number in Parentheses Refers to the Number of Replicates for Each Different Specimen).

(a)

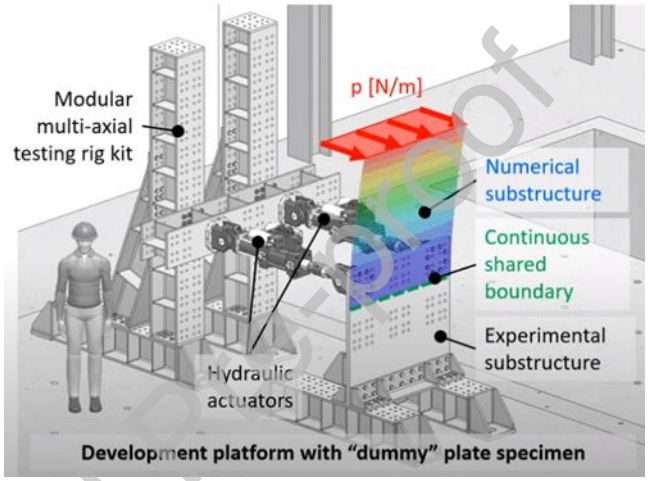

(b)

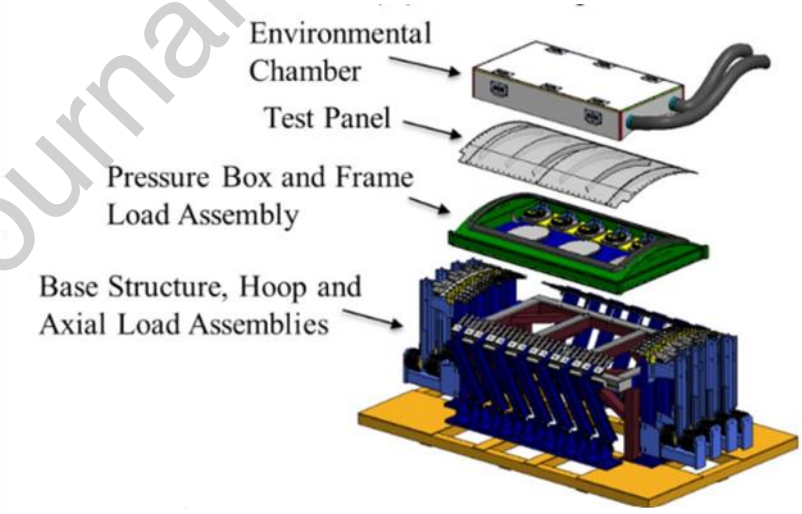

Figure 3: Two examples of direct loading test benches: (a) Modular multi-axial testing rig from CERTEST program, university of Bristol, UK (b): FAA FASTER facility.

(a)

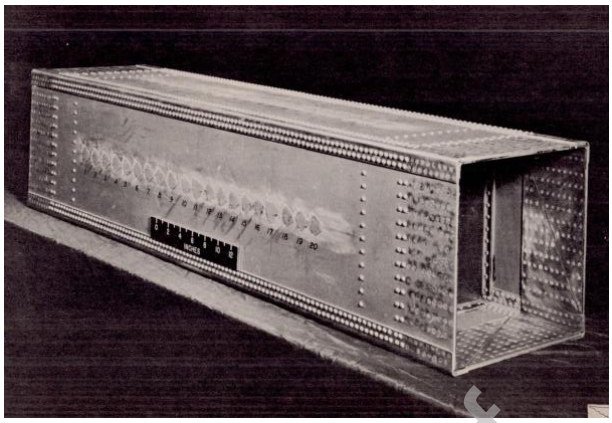

(b)

Figure 4: (a) The very first box for combined loading at NASA Langley 1948 [13] and (b) the first testing bench under combined loading developed by Castanié during his PhD [17, 18].

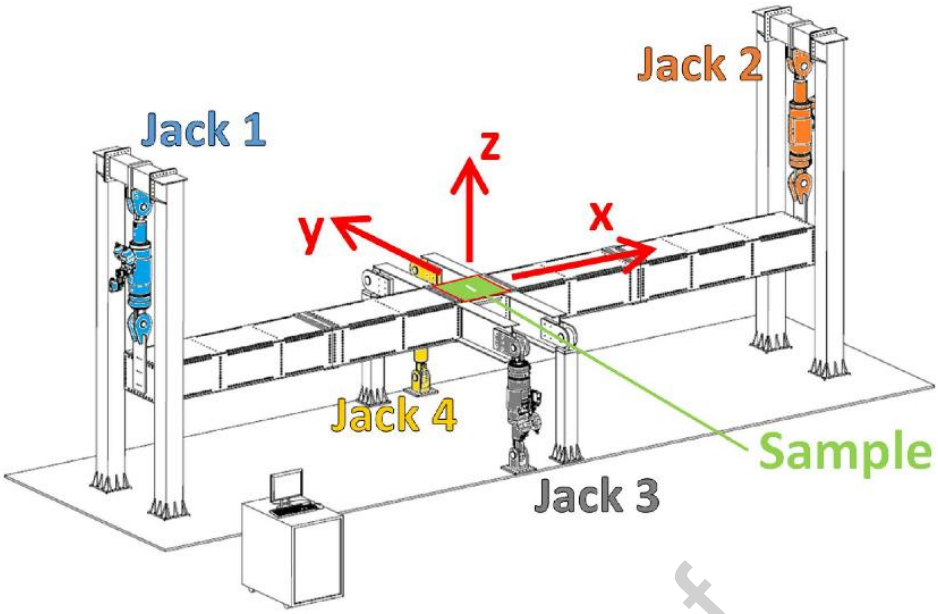

Figure 5: Principle of combined loading with the VERTEX test bench.

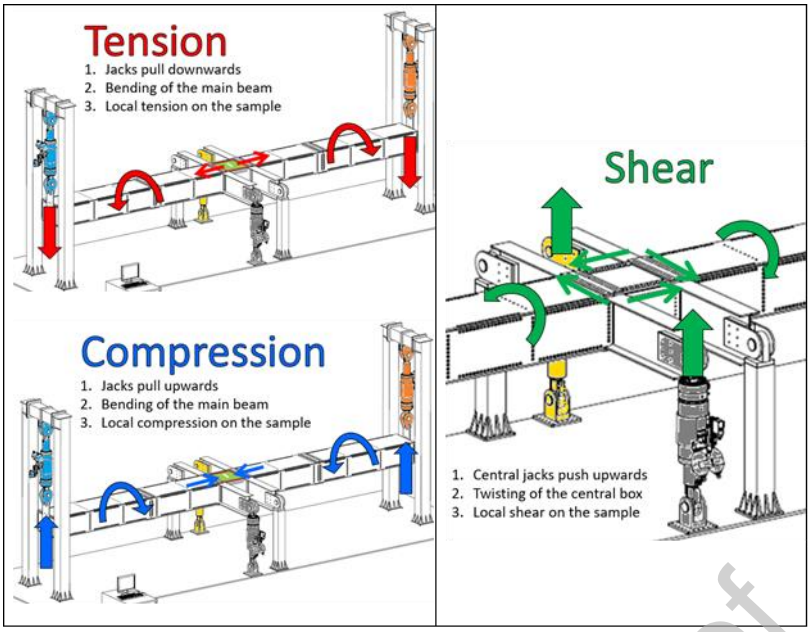

Figure 6: Actuation of the four jacks of the VERTEX test rig to deform the bench and locally apply tension/compression and shear to the sample.

Figure 7: Overview of the VERTEX test bench

(a)  (b) 

Figure 8: Zoom on the bolted area of the sample with 128 bolts (a) and on the air-pressurized rubber bladder (b).

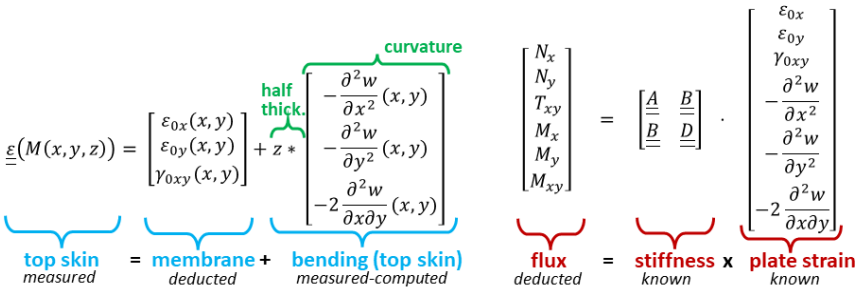

Figure 9: Determination of Force and Moment fluxes from strains obtained with the help of Stereo Digital Image Correlation

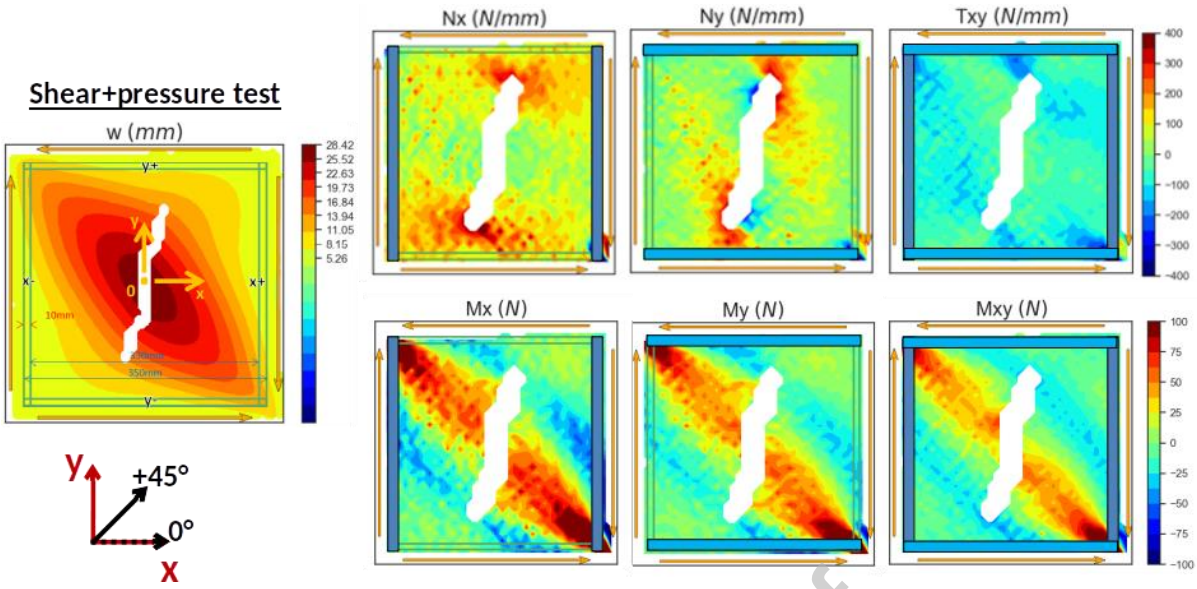

Figure 10: Distribution of force and moments during a *Shear+Tension* test

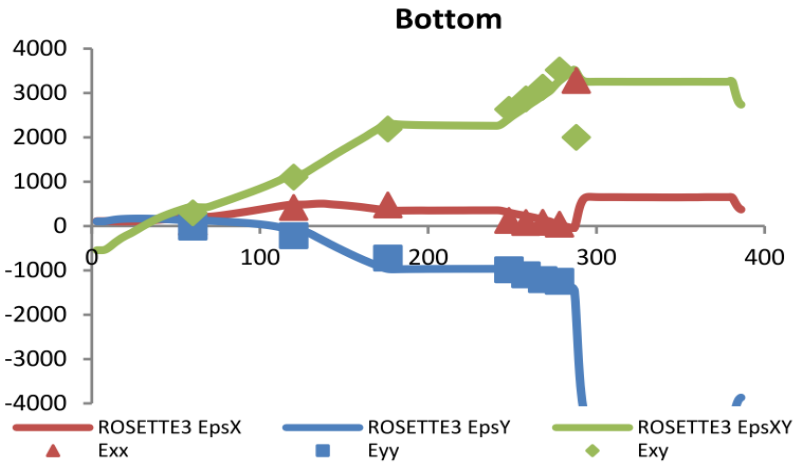

Figure 11. Comparison between strain values on the hidden face of the plate obtained with gauges (solid lines) and extracted from the regularized finite element-stereo digital image correlation measurement (symbols).

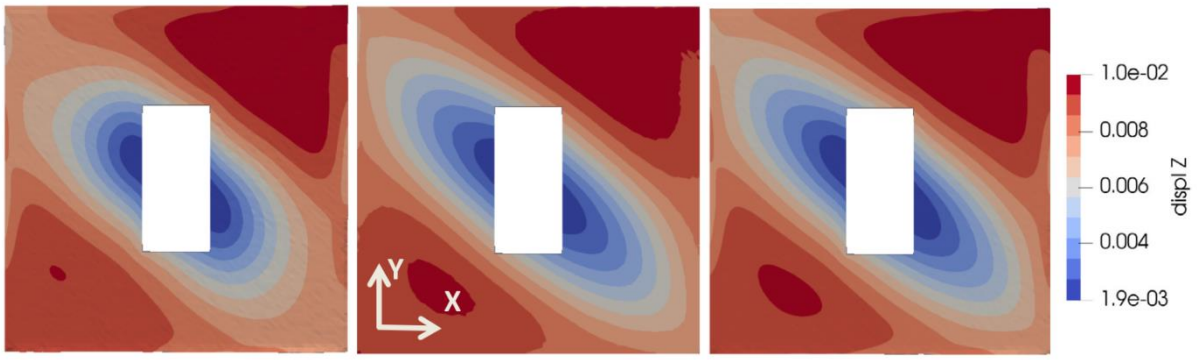

Figure 12. Displacement field in the out-of-plane direction with linear regularization (left) and with non-linear regularization (right). These fields can be compared to the classic FE stereo digital image correlation (SDIC) displacement field (without regularization but without flux estimation) (middle)

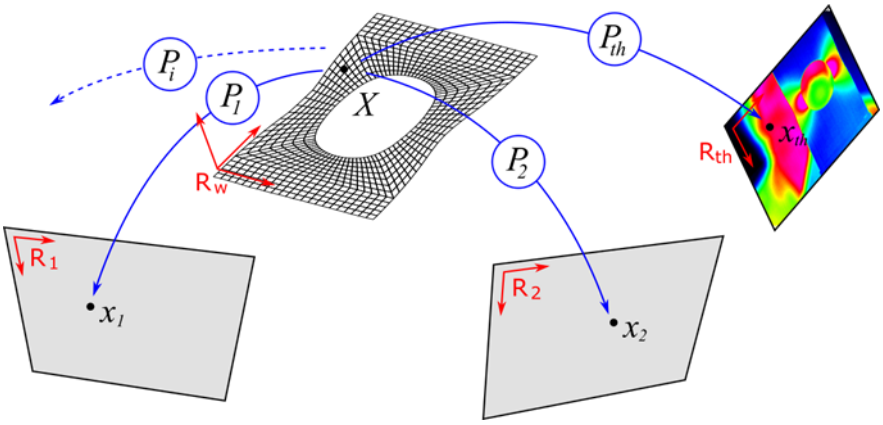

Figure 13. Multimodal setting with numerous visible cameras and one IR camera: Camera models P1, P2 ...Pi and Pth bring the image data back to the part reference frame.

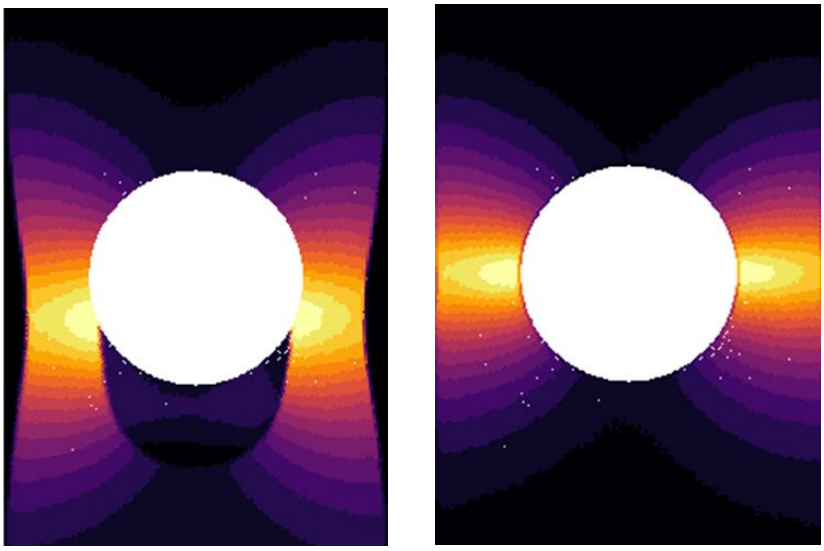

Figure 14. Initial Eulerian temperature field directly extracted for the IR image (left) and the Lagrangian temperature field extracted through the composition of the camera model by the measured transformation (right).

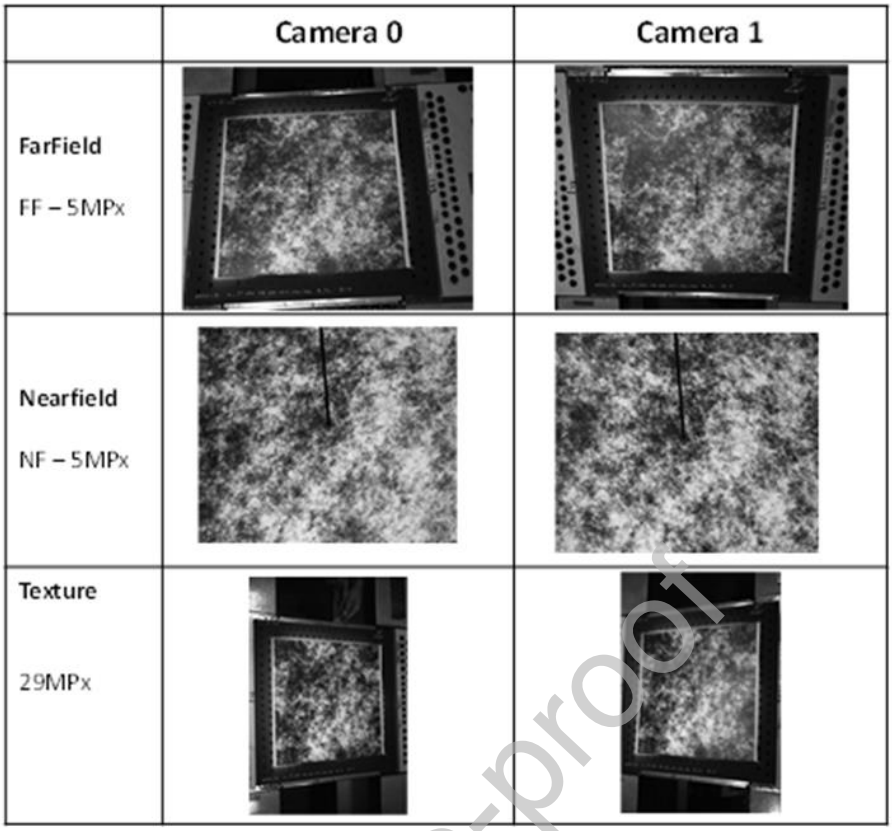

Figure 15: Views from the 6 different cameras used on the VERTEX test rig

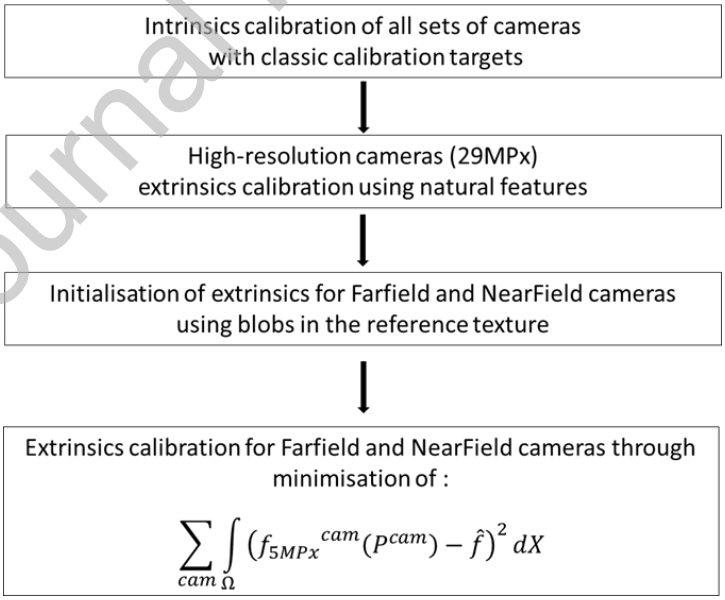

Figure 16: Multi-scale calibration procedure

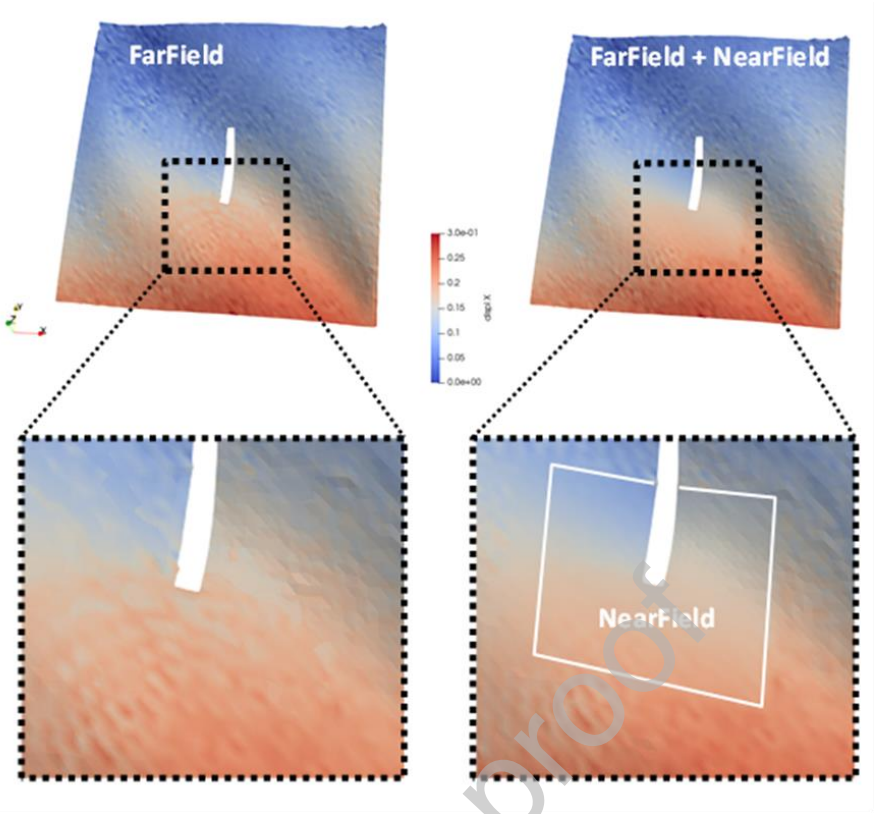

Figure 17: Displacement (×20) along the X-axis focused in a zone around the notch - just before the first failure. Left - 5MPx FF measurement - Right - 5MPx FF+NF measurement.

(b)

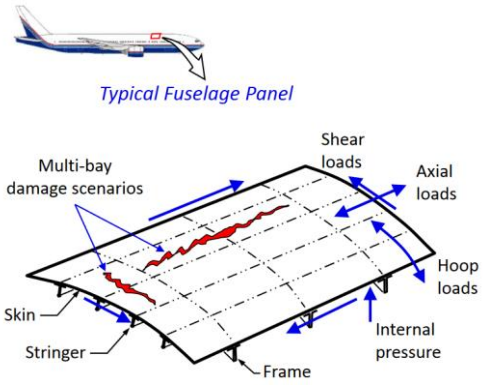

(c)

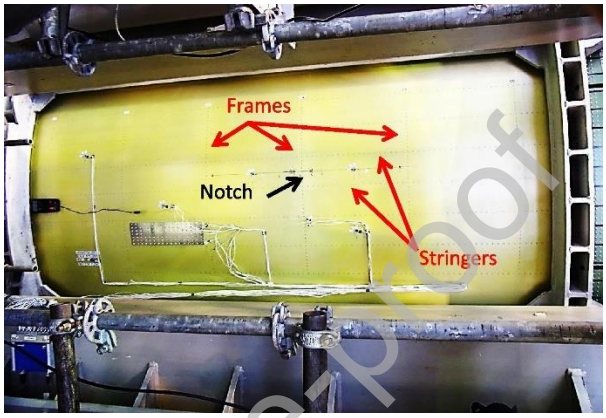

Figure 28: Large damage on fuselage generated by uncontained engine failure ((a) from [39], (b) from [40], (c): Large notch panel full scale test (Courtesy of Airbus).

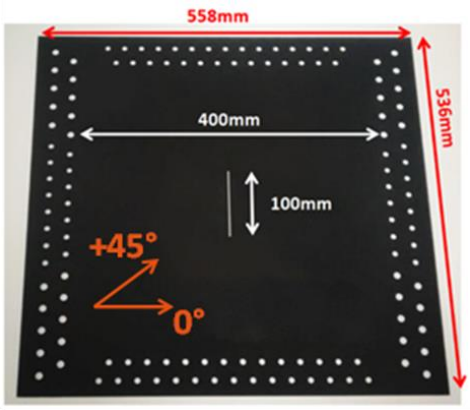

Figure 19: Notched VERTEX specimen geometry.

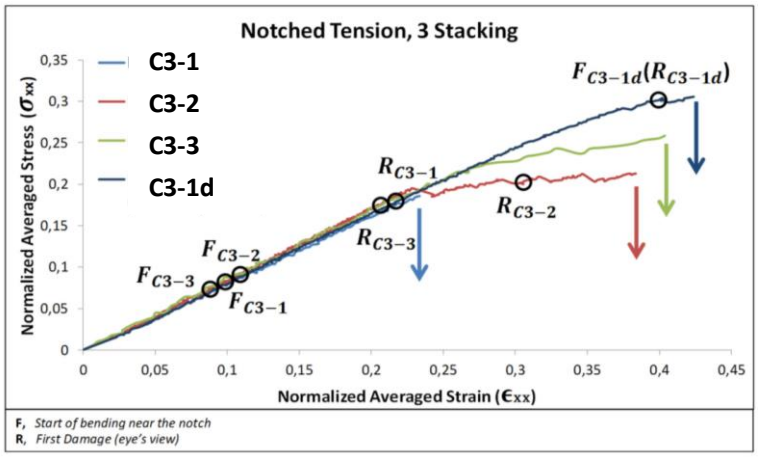

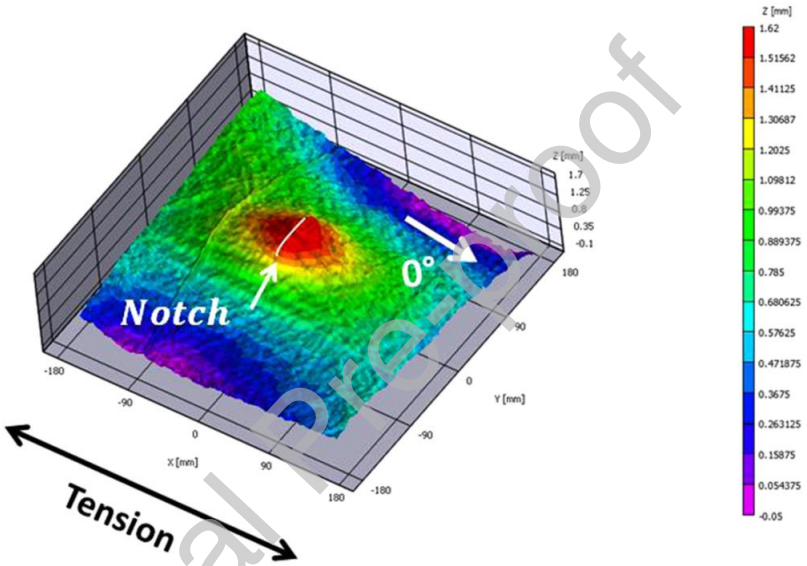

Figure 20: (a) Influence of the stacking sequence and thickness on the notched tensile behavior, (b) Bending around the notch - F_{C3-1} for C3-1 stacking sequence.

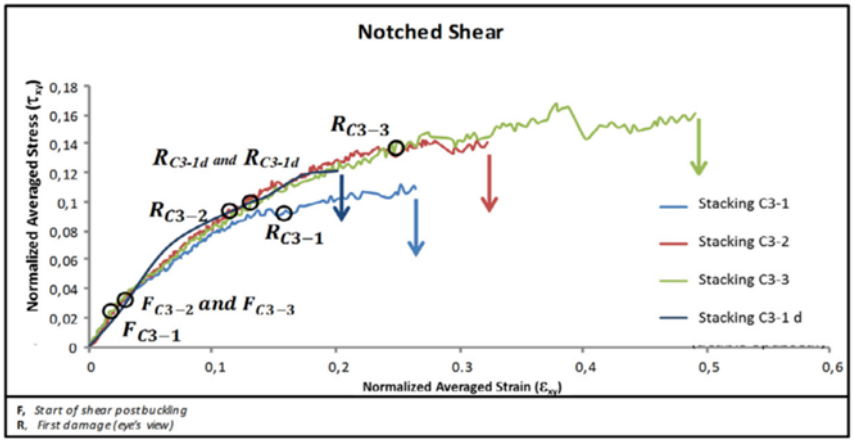

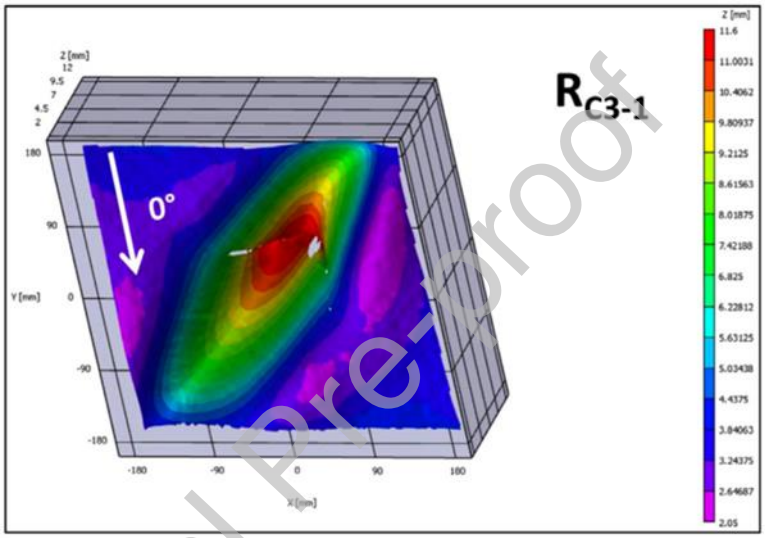

Figure 21: (a) Influence of the stacking sequence and thickness on the notched shear behavior; (b) Bending around the notch - F_{C3-1} for C3-1 stacking sequence.

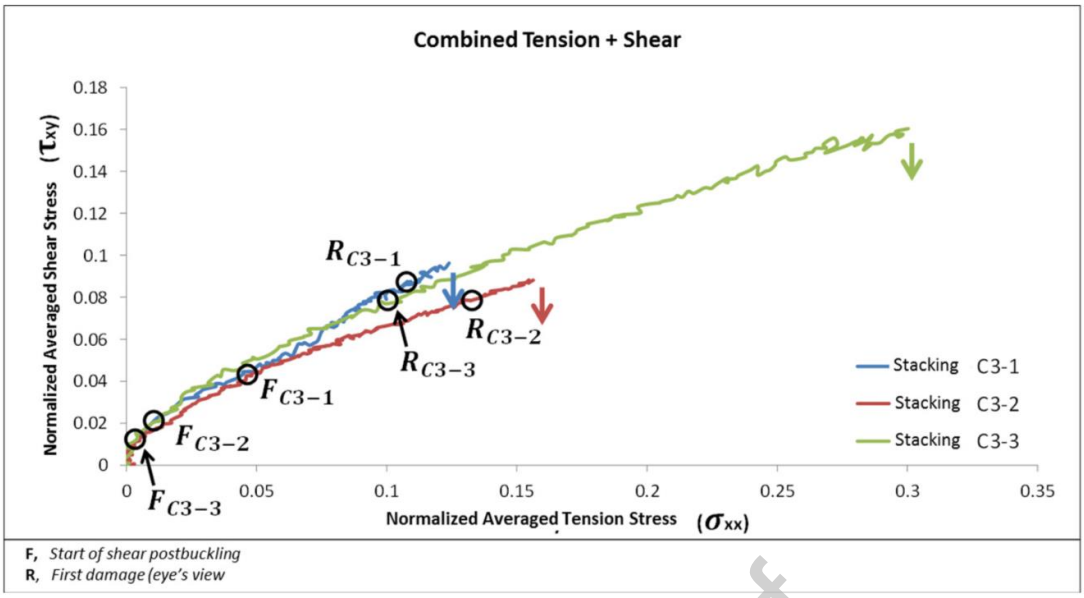

Figure 22: Influence of the stacking sequence on the notched tensile +shear behavior

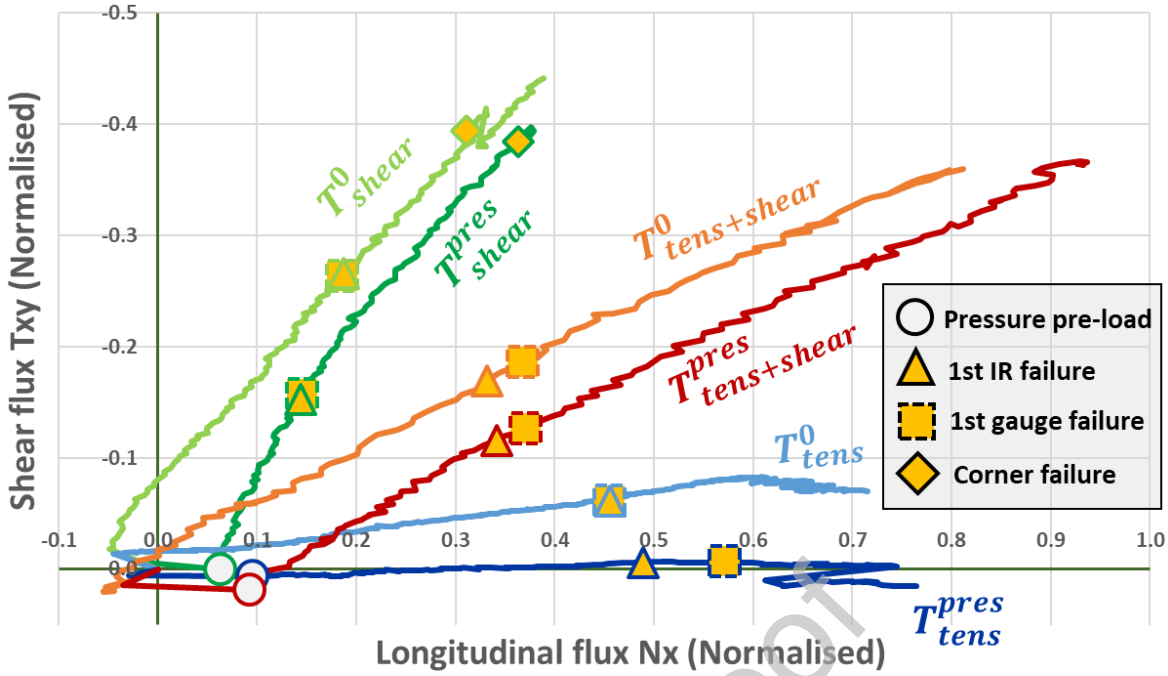

Figure 23: Superposition of computed force flux for each test considered.

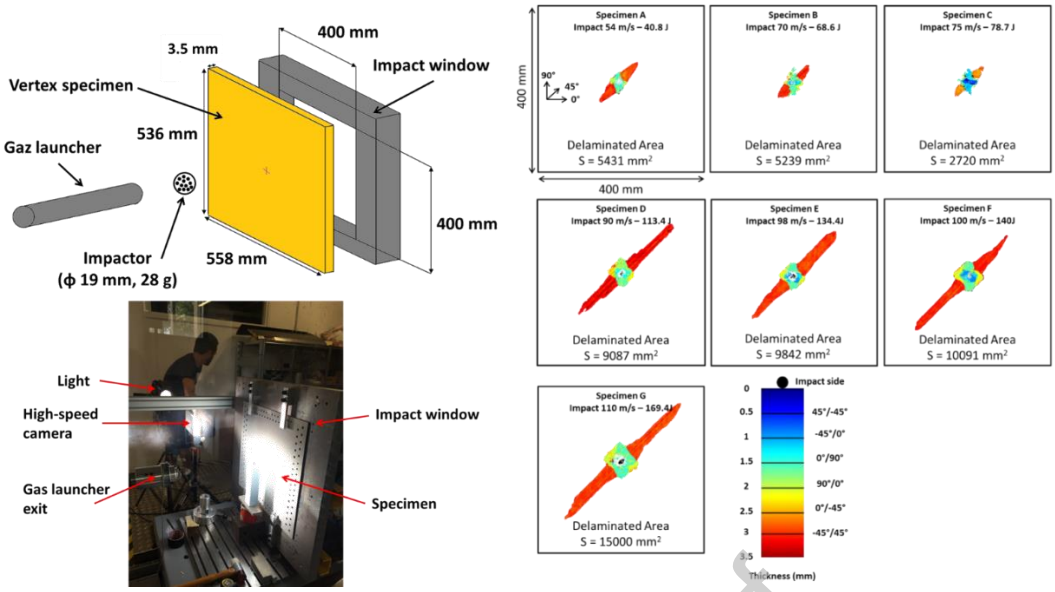

Figure 24. Impact test set-up and Delamination areas obtained by C-Scan after impact for the seven specimens

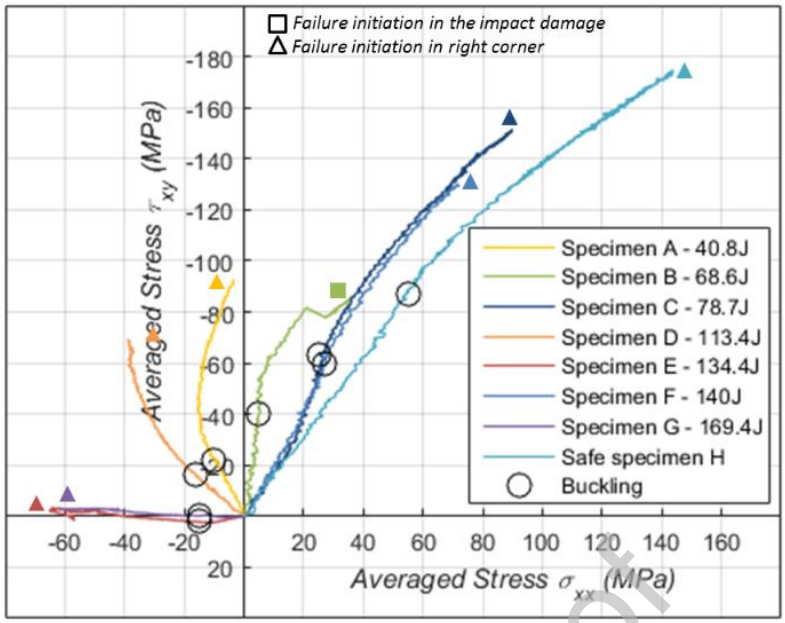

Figure 25. Loading paths for all specimens tested in the VERTEX test rig

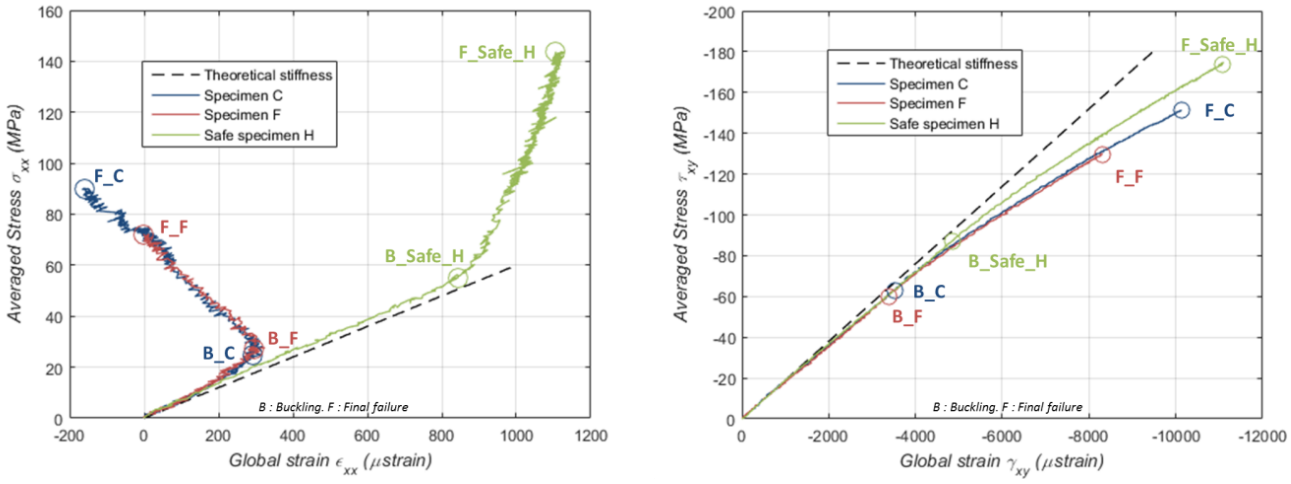

Figure 26. Stress/strain curves for specimens C, F and non-impacted specimen H in tension/shear loading

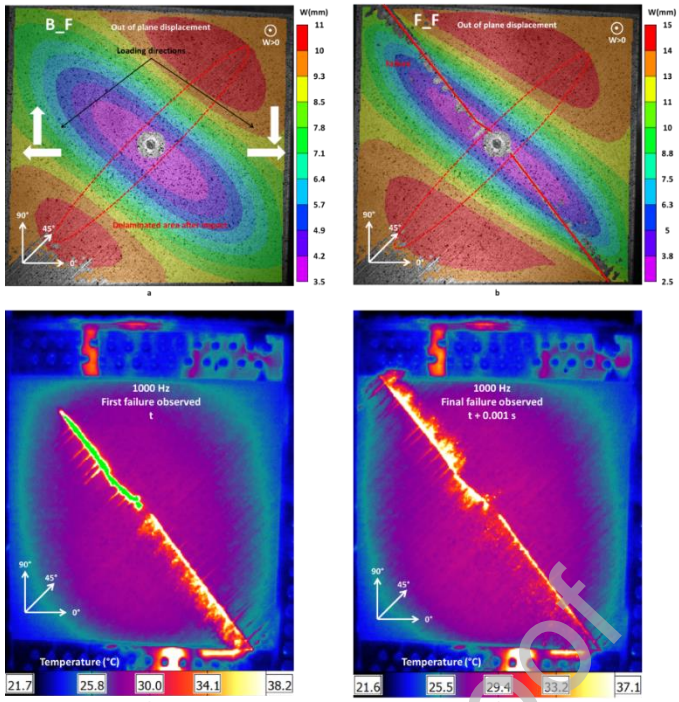

Figure 27. Out-of-plane displacement for specimen F: a – first buckling mode, b – final failure, c – first failure and d – failure propagation observed with thermal camera.

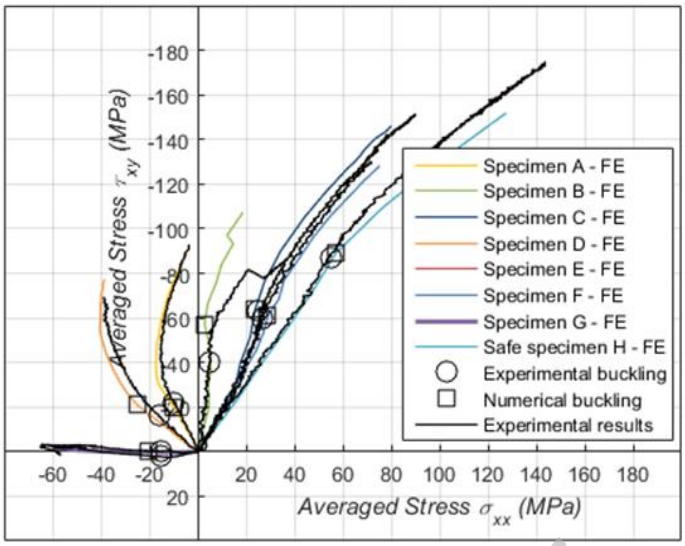

Figure 28. Comparison of numerical and experimental loading paths for all specimens tested in the VERTEX test rig

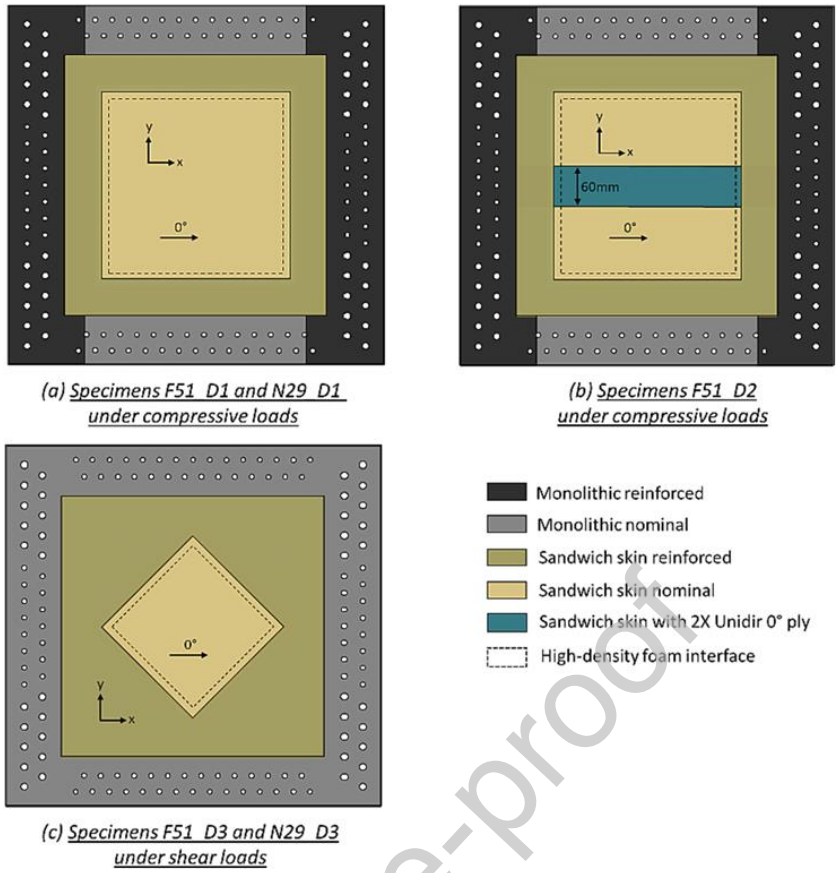

(a) Specimens F51_D1 and N29_D1 under compressive loads

(b) Specimens F51_D2 under compressive loads

(c) Specimens F51_D3 and N29_D3 under shear loads

Figure 29: Definition of the specimen skins.

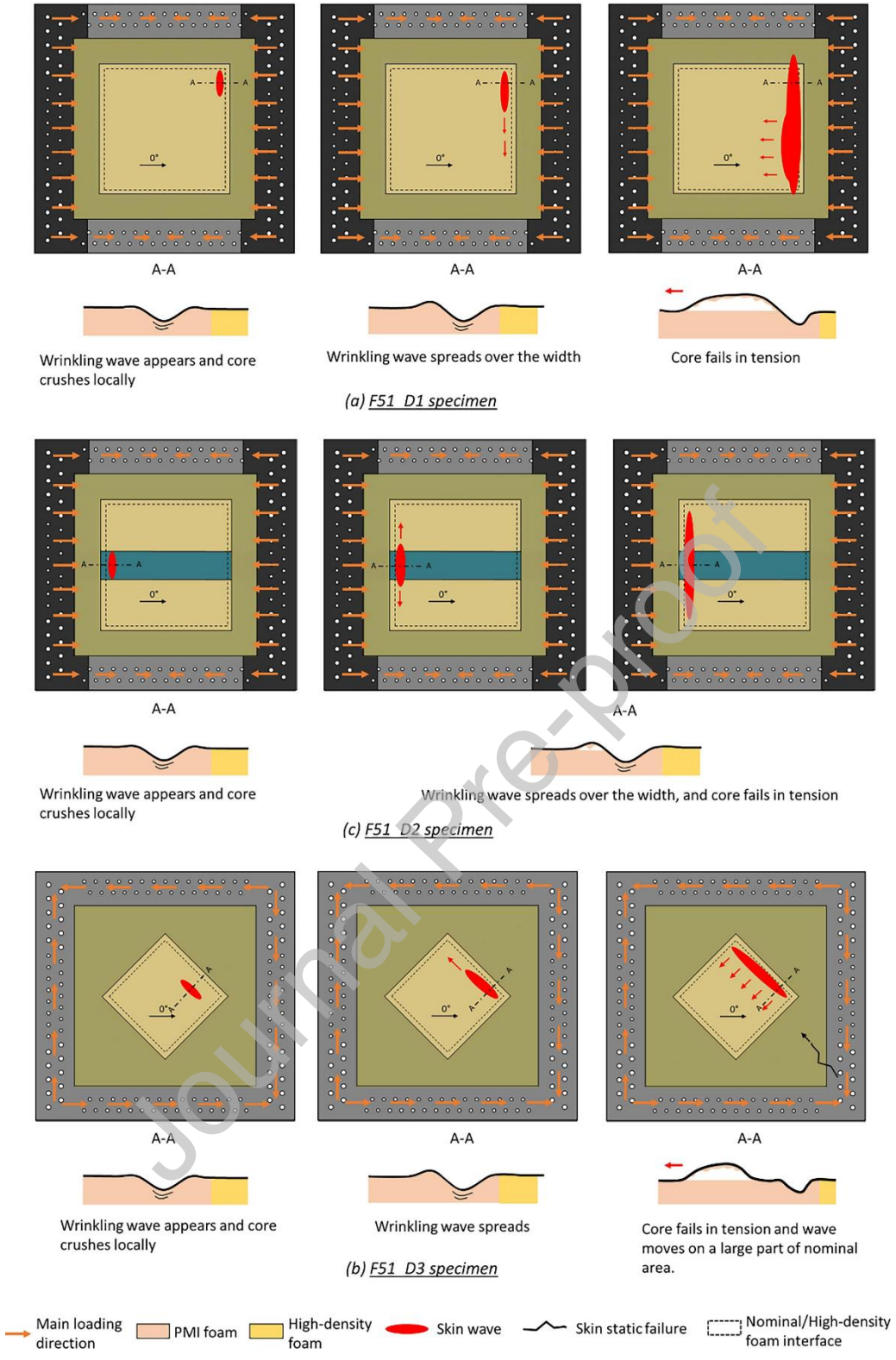

Figure 30. Failure scenario for specimens under compression and shear.

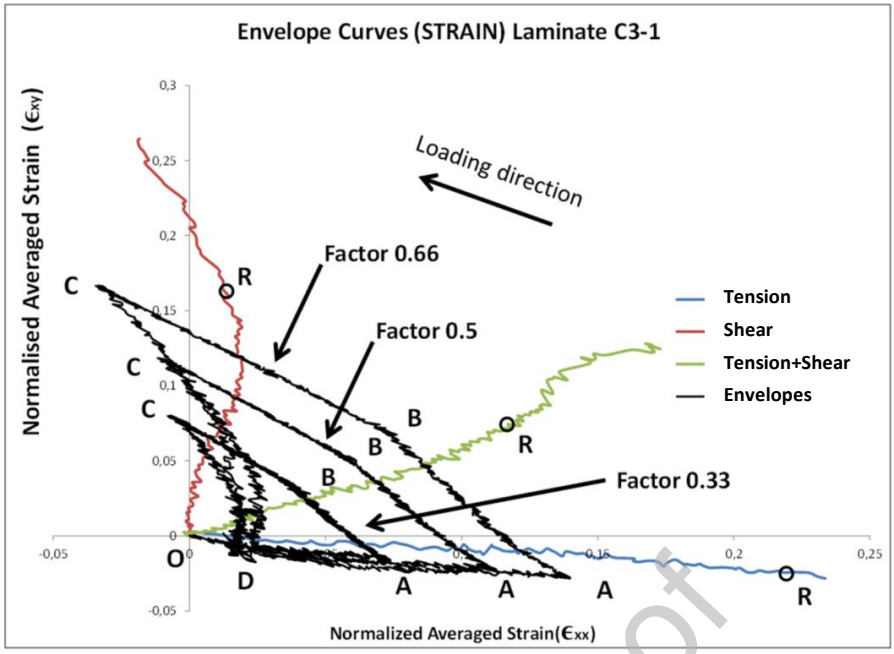

Figure 31: Envelope curve determined using data from previous proportional tests

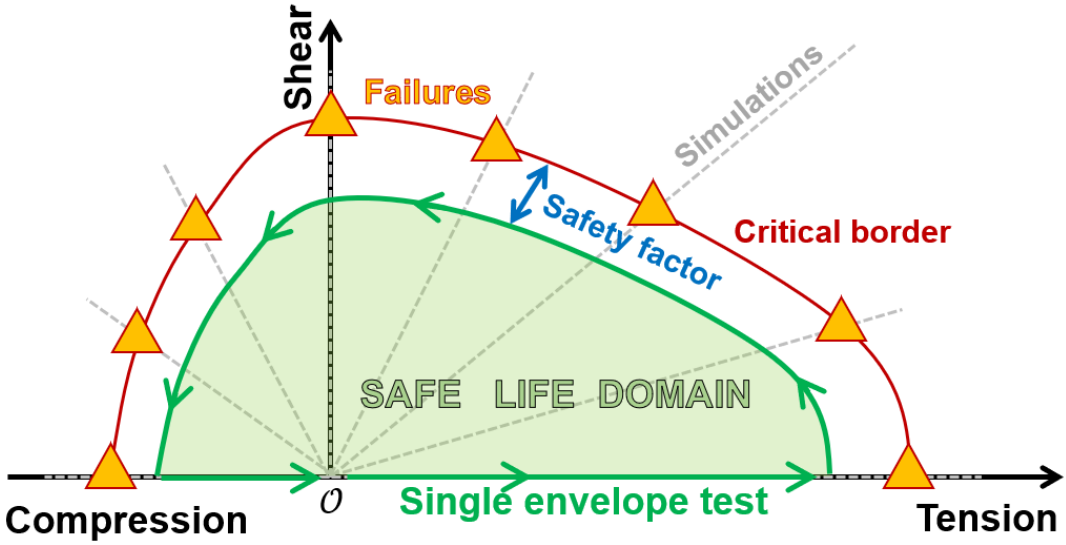

Figure 32: Description of the Safe Life Domain Method to validate a loading domain of a given sample, from numerical simulations and a single envelope test.

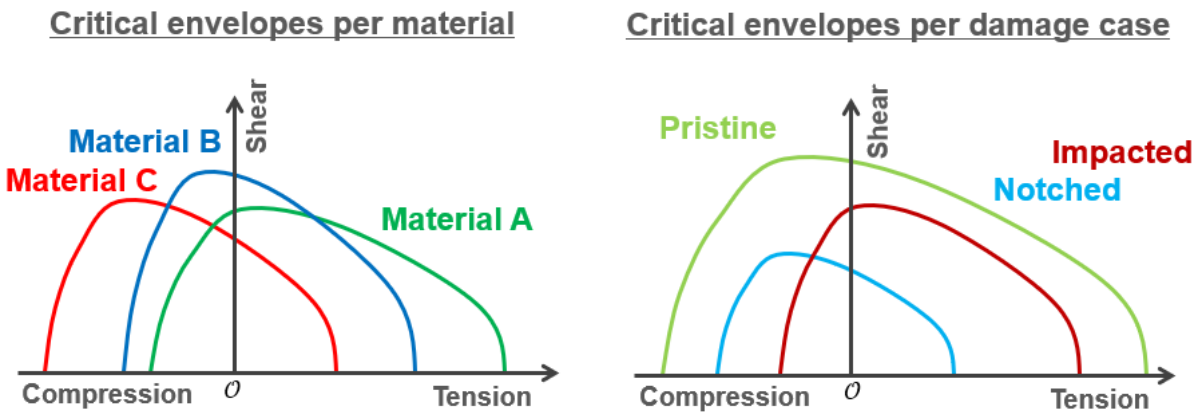

Figure 33: Illustration of stacked critical envelopes on a given specimen – (left) for various pristine materials – (right) for various load cases on a given material.

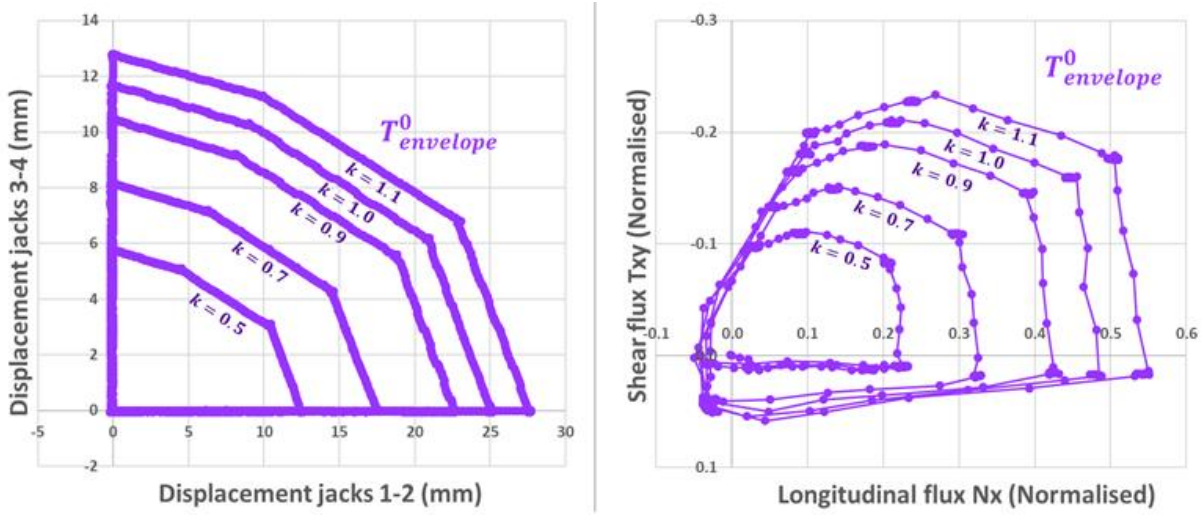

Figure 34: Representation of the $T^0_{envelope}$ test through two loading spaces: (left) imposed displacement on jacks, (right) force flux on the sample. For imposed shear displacements, the Wagner effect leads to tension+shear on the sample [7].

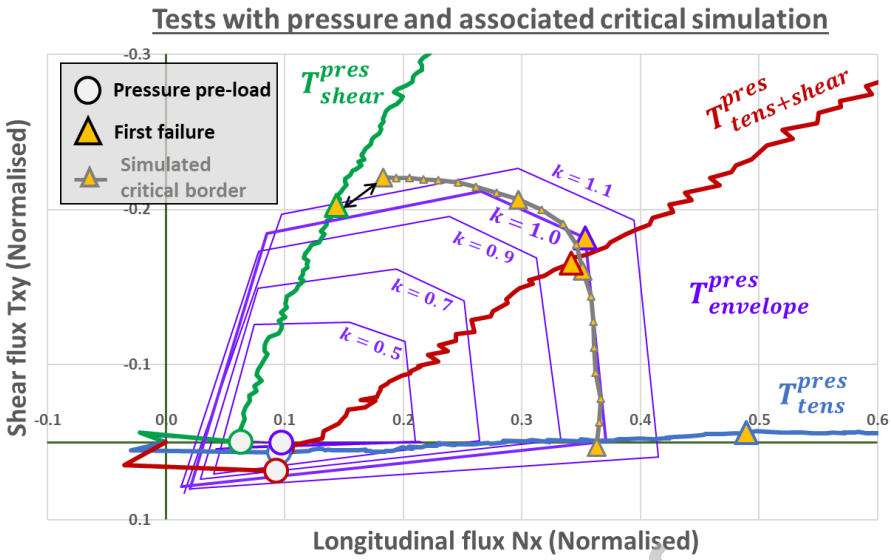

Figure 35: Superposition of flux curves for each test and the critical envelope simulation with pressure.

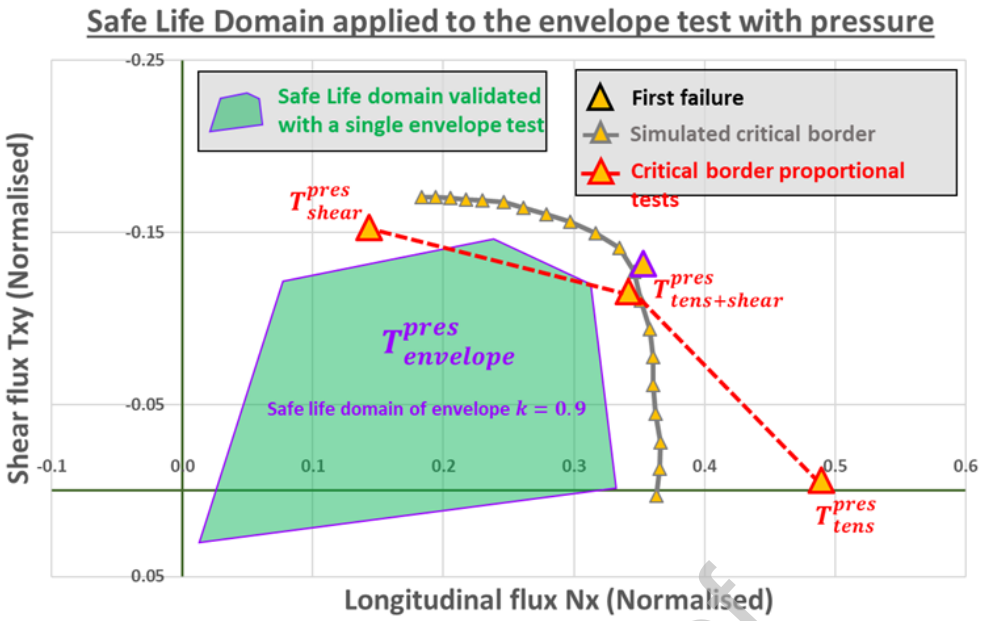

Figure 36: Safe Life Domain application to the last safe envelope of $T^{pres}_{envelope}$, compared to the simulated critical border and the indicative experimental failure of proportional tests.

12. Tables

Table 1. Overview of impact results and loading path

Specimen	*Velocity (m/s)*	*Impact Energy (J)*	*Delaminated Area (mm^2)*	*Loading after Impact*
A	*54*	*40.8*	*5431*	*Compression/shear*
B	*70*	*68.6*	*5239*	*Shear*
C	*75*	*78.7*	*2720*	*Shear/tension*
D	*90*	*113.4*	*9087*	*Compression/shear*
E	*98*	*134.4*	*9842*	*Compression*
F	*100*	*140*	*10091*	*Shear/tension*
G	*110*	*169.4*	*15000*	*Compression*
H	*-*	*-*	*0*	*Shear/tension*

Table 2: Stacking sequence for specimens in nominal area. Specimen nomenclature is F51_… or N29_… for PMI foam or NOMEX® honeycomb respectively and …_Dx for specified stacking sequence.

Specimen	F51_D1	N29_D1	F51_D2	F51_D3	N29_D3
Loading	Compressive	Compressive	Compressive	Shear	Shear
Stacking sequence	Fabric +/- 45°	Fabric +/- 45°	Fabric +/- 45°	Fabric +/- 45°	Fabric +/- 45°
			2 x Unidir 0°		
	Fabric 0°/90°	Fabric 0°/90°	Fabric 0°/90°	Fabric +/- 45°	Fabric +/- 45°
	adhesive film	adhesive film	adhesive film	adhesive film	adhesive film
	PMI foam	NOMEX® honeycomb	PMI foam	PMI foam	NOMEX® honeycomb
	adhesive film	adhesive film	adhesive film	adhesive film	adhesive film
	Fabric 0°/90°	Fabric 0°/90°	Fabric 0°/90°	Fabric +/- 45°	Fabric +/- 45°
	Fabric +/- 45°	Fabric +/- 45°	Fabric +/- 45°	Fabric +/- 45°	Fabric +/- 45°
				Fabric +/- 45°	Fabric +/- 45°

Declaration of interests

☒ The authors declare that they have no known competing financial interests or personal relationships that could have appeared to influence the work reported in this paper.

☐The authors declare the following financial interests/personal relationships which may be considered as potential competing interests:

Bruno Castanié, Jean-Charles Passieux, Jean-Noel Périé, Christophe Bouvet, John-Eric Dufour and Joël Serra